

JGR Earth Surface

RESEARCH ARTICLE

10.1029/2022JF006967

Key Points:

- We use knickpoint travel time to estimate the time between knickpoint passage and channel/hillslope adjustments to accelerated incision
- The adjustment of channel width after the passage of a knickpoint takes $>10^5$ years since the passage of a slope-break knickpoint
- Adjustment of the entire river basin takes much longer than the knickpoint travel time to the channel heads

Supporting Information:

Supporting Information may be found in the online version of this article.

Correspondence to:

N. O. Takahashi and J. B. H. Shyu,
naoya.takahashi.c5@tohoku.ac.jp;
jbhs@ntu.edu.tw

Citation:

Takahashi, N. O., Shyu, J. B. H., Toda, S., Matsushi, Y., Ohta, R. J., & Matsuzaki, H. (2023). Transient response and adjustment timescales of channel width and angle of valley-side slopes to accelerated incision. *Journal of Geophysical Research: Earth Surface*, 128, e2022JF006967. <https://doi.org/10.1029/2022JF006967>

Received 19 OCT 2022

Accepted 27 JUN 2023

Author Contributions:

Conceptualization: Naoya O. Takahashi

Formal analysis: Naoya O. Takahashi

Investigation: Naoya O. Takahashi, Yuki Matsushi, Ryoga J. Ohta, Hiroyuki Matsuzaki

Methodology: Naoya O. Takahashi

Resources: Yuki Matsushi, Ryoga J. Ohta, Hiroyuki Matsuzaki

Supervision: J. Bruce H. Shyu, Shinji Toda

Writing – original draft: Naoya O. Takahashi

Writing – review & editing: J. Bruce H. Shyu, Shinji Toda, Yuki Matsushi, Ryoga J. Ohta

© 2023. American Geophysical Union.
All Rights Reserved.

Transient Response and Adjustment Timescales of Channel Width and Angle of Valley-Side Slopes to Accelerated Incision

Naoya O. Takahashi¹ , J. Bruce H. Shyu² , Shinji Toda³ , Yuki Matsushi⁴, Ryoga J. Ohta⁵ , and Hiroyuki Matsuzaki⁶

¹Department of Earth Science, Tohoku University, Sendai, Japan, ²Department of Geosciences, National Taiwan University, Taipei, Taiwan, ³International Research Institute of Disaster Science (IRIDeS), Tohoku University, Sendai, Japan, ⁴Disaster Prevention Research Institute, Kyoto University, Uji, Japan, ⁵Faculty of Science and Engineering, Chuo University, Tokyo, Japan, ⁶Micro Analysis Laboratory, Tandem Accelerator (MALT), The University Museum, The University of Tokyo, Tokyo, Japan

Abstract Studying bedrock rivers during their transient states helps understand the response of a fluvial system to the changing boundary conditions. Although theoretical studies predict how river form adjusts to changes in incision or rock uplift rates, field constraints on the timescale of this adjustment are limited. We investigated the transient behavior of channels and hillslopes and estimated the adjustment times of channel width and angle of valley-side slopes to accelerated incision based on knickpoint travel time. We documented channel slopes, channel widths, and hillslope angles along six rivers around an active normal fault in Iwaki, Japan, and identified river sections in a transient state. Channel slopes and basin-averaged erosion rates determined from ¹⁰Be concentrations are distinct between rivers near and distant from the fault, suggesting that past increases in fault throw rates triggered the knickpoint formation and the observed transient response. Adjustment time for width is at least 10^5 years and can take 10^6 years after the knickpoint passage. Adjustment time for hillslope angles is generally shorter than for channel width. However, the hillslope adjustment may take longer than previously reported if the effect of width adjustment on hillslope angles is significant or the complete adjustment of hillslope angles is considered. The fact that channel slope, channel width, and hillslope angle have distinct adjustment times underlines the importance of correctly identifying river sections that are fully adjusted to the new boundary conditions when inferring erosion or relative uplift rates for bedrock rivers.

Plain Language Summary Bedrock rivers adjust their forms in response to changes in geologic and climatic conditions, such as underlying rock types, tectonics, and precipitation, which means that establishing their quantitative relationships between these conditions may enable us to infer rates of erosion or relative uplift by studying fluvial landscape. Although it is well known how river and hillslope forms adjust after an increase in erosion rates, the timescale of these adjustments is difficult to constrain in an actual landscape. This study presents a method to estimate the adjustment times of channel width and hillside slope angles along the sides of a valley. We studied a set of rivers that cross an active normal fault and documented the variations of channel and hillslope forms along their courses. These rivers are now changing their shapes after motion on the fault has increased their erosion rates. Our analysis shows that channel width continues to change for $>10^5$ years following an increase in erosion rates. Changes in hillslope angles take less time than changes in channel width. Our findings show that channel slope, channel width, and hillslope angle all have distinct adjustment times to increase erosion rates.

1. Introduction

Because the incision of rivers into bedrock is a major element in the formation of mountain landscapes, quantifying incision rates and their relationships with external forcing is important for understanding landscape evolution. The morphologies of channel and hillslope are closely related to erosion rates, and a long history of research has gone into establishing their functional relationships (e.g., Ahnert, 1970; Kirby & Whipple, 2012; Roering et al., 2007; Wobus et al., 2006). A sudden increase in the rates of base-level fall (i.e., relative uplift) can enhance local incision rates and may generate a knickpoint that migrates upstream (e.g., Crosby & Whipple, 2006; Whipple & Tucker, 1999). As it does so, channels and hillslopes along its passage gradually adjust their forms to the accelerated incision rates. Knickpoints are common in tectonically active areas, and thus knowledge of the

transient response of rivers to an increase in incision rates may enable researchers to infer a region's erosional or tectonic history from river morphologies (Goren et al., 2014; Rudge et al., 2015; Wang et al., 2022).

Channel slope, channel width, and the angle of valley-side slopes are closely related to channel incision rates, and many studies have reported the transient response of channels and hillslopes to changes in incision rates (e.g., Lavé & Avouac, 2001; Montgomery & Brandon, 2002; Reinhardt et al., 2007; Roering et al., 2001; Snyder et al., 2000; Whipple & Tucker, 1999; Yanites & Tucker, 2010). The channel steepness index (e.g., Snyder et al., 2000), expressing the channel slope divided by upstream drainage area to the power of the channel concavity, increases after the passage of a knickpoint in response to an increase in incision rates. Channel steepness downstream from the migrating knickpoint is assumed to reach a new steady-state value and is often positively correlated with uplift rates (e.g., Chen et al., 2015; Gallen & Wegmann, 2017; Kirby & Whipple, 2012; Regalla et al., 2013). Channel width can become wider or narrower in response to increased incision rates or be insensitive to incision rates (e.g., Lavé & Avouac, 2001; Snyder et al., 2003; Whittaker et al., 2007; Yanites & Tucker, 2010; Zhang et al., 2017). According to a numerical study that considered the effects of sediment cover, channel narrowing occurs after the knickpoint passage, but as the knickpoint travels upstream, the local sediment supply continues to increase, resulting in gradual widening of the channel (Yanites, 2018). Baynes et al. (2022) conducted flume experiments and reported width evolution during knickpoint retreat. They found that width decreased upstream of the knickpoint and reached the minimum at the knickpoint, and then increased after the passage of the knickpoint. Hillslope morphology is set by river incision at its base. The hillslope angle increases with incision rates until it reaches a threshold angle, above which it becomes insensitive to incision rate (e.g., Montgomery & Brandon, 2002). The threshold angle, usually 30°–40°, is reached at surface-lowering rates of 0.2–1.0 mm/yr (e.g., DiBiase et al., 2012; Montgomery & Brandon, 2002; Ouimet et al., 2009). Also, hilltop curvature increases with incision rates and continues to be coupled with incision rates after the hillslope angle attains the threshold (e.g., Hurst et al., 2012; Roering et al., 2007).

Although many studies have examined how river morphologies adjust to changes in incision rates, relatively few have attempted to quantify the adjustment timescales of channels and hillslopes to accelerated incision. Such studies require a chronology that specifies the times at which these morphological adjustments begin and end. In actual landscapes, more studies have been conducted to constrain adjustment timescales of channel slope than those of channel width and hillslope angles (e.g., Crosby & Whipple, 2006; Whittaker & Boulton, 2012). The arrival of a knickpoint triggers a change in channel slope from which the rate of knickpoint retreat can be calculated (e.g., Royden & Perron, 2013; Whipple & Tucker, 1999). Therefore, when the time and place at which a knickpoint is generated are known, the timescale of channel slope adjustment can be estimated based on the knickpoint's travel distance and travel speed (e.g., DiBiase et al., 2015).

The adjustment timescales of channel width and hillslope angle, unlike that for channel slope, are difficult to estimate from field evidence alone. Instead, they have been studied by numerical modeling with parameters calibrated by field evidence (e.g., Attal et al., 2008; Hurst et al., 2012; Mudd & Furbish, 2007; Roering et al., 2001; Turowski, 2020; Yanites, 2018). Attal et al. (2008) examined the transient response of a catchment to an increase in fault throw rates and discussed the impact of dynamic width adjustment on channel slope adjustment and the response time of a catchment. They modeled channel width as a function of stream discharge and channel slope and implicitly assumed that channel width was instantly adjusted to the increased incision rates when the knickpoint passed. Therefore, the width adjustment occurred at the same time as the arrival of the knickpoint and took virtually no time. Yanites (2018), modeled the evolution of channel width after knickpoint passage. The results showed that width adjustment can lag behind knickpoint passage and could take 10^5 – 10^6 years depending on the incision model and the conditions of sediment transport (e.g., detachment-limited condition). Roering et al. (2001) used sediment transport models on hillslopes to estimate the adjustment time of valley-side slopes to a change in base-level-lowering rates. They demonstrated that the adjustment time of hillslopes is less than 50 kyr in the Oregon Coast Range, similar to the adjustment timescale reported in the Feather River basin in California (Hurst et al., 2012). However, we still know little about the actual adjustment timescales of channel width and hillslopes due to the difficulties in constraining when those adjustments started and finished.

Interactions between channels and hillslopes must be considered to understand the response of channels and hillslopes to a base-level change (e.g., Baynes et al., 2022; Gallen et al., 2011; Golly et al., 2017; Hurst et al., 2019; Reinhardt et al., 2007; Yanites, 2018). A rapid incision following the passage of a knickpoint cuts hillslope toes, leading to bank failure and steepening of hillslopes (Gallen et al., 2011; Golly et al., 2017; Reinhardt et al., 2007).

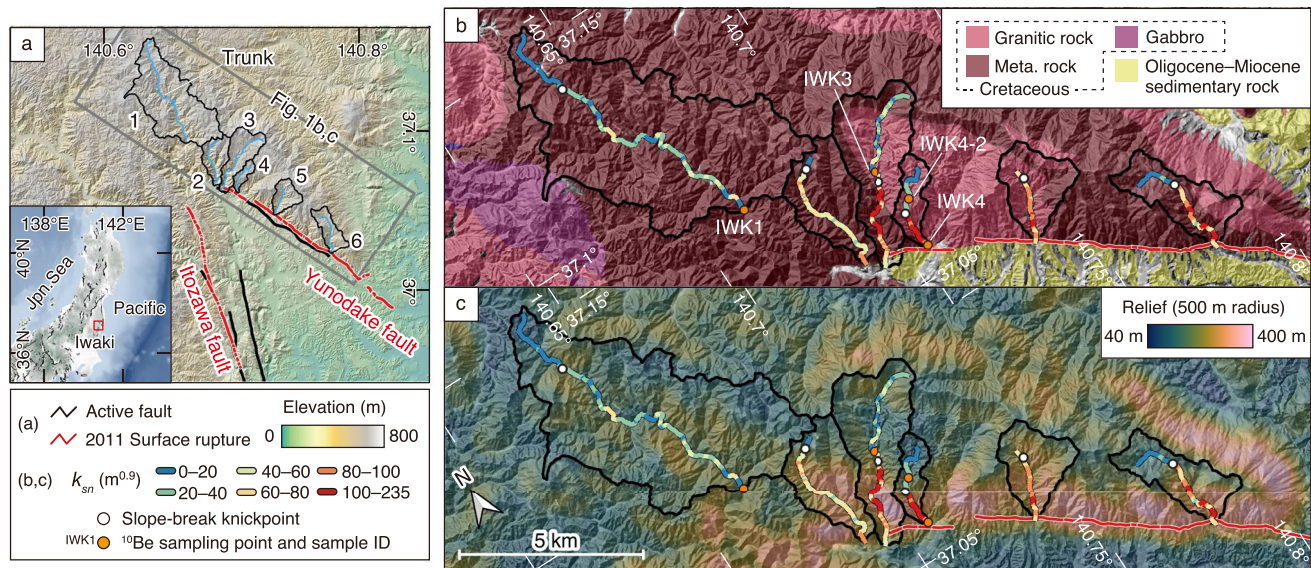


Figure 1. (a) Location and topography of the study area. Drainage basins and their trunk streams are labeled with their identification number (1–6). The inset map shows topography and active fault traces in eastern Japan. Active fault traces are from Nakata & Imaizumi (2002). Surface rupture traces are after Toda & Tsutsumi (2013). (b) Geologic map around the Yunodake fault (Geological Survey of Japan, 2020; Kubo et al., 2007). (c) Topographic relief in the area of (b) within circular windows of 500 m radius.

Channel narrowing can occur near the migrating knickpoint, and then widening follows due to the increased sediment supply as the knickpoint travels upstream (Yanites, 2018). Channel widening following the knickpoint retreat decreases hillslope lengths and causes further steepening of hillslopes (Baynes et al., 2022). These studies demonstrated the tight coupling of channels and hillslopes and highlighted the need to investigate the co-evolution of channels and hillslopes during a retreat of a knickpoint.

This study examines the transient response and adjustment timescales of channel width and hillslope angles to increased incision rates. We present a method to quantify the adjustment timescales of channel width and the angle of valley-side slopes based on knickpoint travel time. We applied the method to bedrock rivers that cross an active normal fault near the city of Iwaki, Japan. Because changes in channel width and hillslopes follow the passage of a knickpoint, we can use knickpoint travel times to estimate three quantities at any given location: response time, the time between the start and finish of a morphological adjustment; delay time, the lag time between the knickpoint arrival and the start of morphological adjustment; and adjustment timescale, the sum of response and delay times, representing the time between knickpoint passage and the completion of adjustment. Because we cannot know exactly when channel or hillslope adjustments have finished, we defined the end of adjustment as the condition where channel and hillslope forms are indistinguishable from those presumably at a steady state. For the adjustment of channel slopes, the delay time at a given location is always zero, the response time is the time from the knickpoint passage until the channel slope attains a steady-state value, and the adjustment time equals the response time. We investigated channel slope, channel width, and hillslope angles along trunk streams and identified points at which morphological adjustments started and finished based on a Bayesian change point analysis. We then calculated knickpoint travel times and estimated the response and delay times of channel width and hillslope angles. We use these results to discuss how the channel width and the angle of valley-side slopes change following an increase in channel incision rates, highlighting the need to inspect channels and hillslopes along a trunk stream and its tributaries when inferring incision or tectonic histories from river morphologies.

2. Background

2.1. Tectonic and Geologic Background

Iwaki is in the Tohoku region of northeastern Japan, which is subjected to E-W compression due to westward subduction of the Pacific plate under the Eurasia plate (Figure 1a). Although most earthquakes in Tohoku are

characterized by reverse faulting, analysis of microearthquakes during 2003–2010 has revealed that the Iwaki area has been in an extensional stress regime since before the 11 March 2011 Mw 9.0 Tohoku-Oki earthquake (Imanishi et al., 2012). Shortly after the Tohoku-Oki event, a normal-faulting event of Mw 6.6 occurred in Iwaki on 11 April 2011. This earthquake produced surface ruptures along the Yunodake and Itozawa faults (Figure 1a) (e.g., Fukushima et al., 2013; Toda & Tsutsumi, 2013). The Yunodake and Itozawa faults are normal faults dipping SW and WSW, respectively. The Yunodake fault was first formed during Eocene-Oligocene, and a half-graben developed at the hanging wall of the fault (Mitsui, 1971), suggesting that this area has experienced extension on a geological timescale. The throw rate of the Yunodake fault is unknown. A paleoseismic trenching study (Miyashita, 2018) showed that three surface-rupturing earthquakes including the 2011 event occurred on the Yunodake fault within the last 7 ky. If we assume that each of these produced vertical displacements similar to that in 2011 (~80 cm: Toda & Tsutsumi, 2013), a rough estimate of the fault throw rate is 0.3–0.4 mm/yr.

Bedrock around the Yunodake fault consists of metamorphic and granitic rocks of Cretaceous age and sedimentary rocks of Miocene age (e.g., Kubo et al., 2007) (Figure 1b). Cretaceous metamorphic rocks include siliceous, mafic, pelitic and calcareous rocks (Hiroi et al., 1987; Kano et al., 1973; Kubo et al., 2007). Cretaceous granodiorite and porphyritic granodiorite occur along the middle and eastern parts of the Yunodake fault (Kubo et al., 2007). Miocene sedimentary rocks southwest of the Yunodake fault include marine and nonmarine clastic rocks (Kubo et al., 2007) that overlie Cretaceous metamorphic rocks (Mitsui, 1971).

We focus on trunk streams of the six drainage basins, numbered 1 through 6, around the Yunodake fault (Figure 1). These drainage basins were selected based on accessibility and drainage areas of trunk and tributary streams. Drainage areas of tributaries are important because a more continuous downstream increase in contributing areas is favored when fitting the hydraulic scaling between width and drainage area to measured channel width. The drainage areas range from 1.6 to 24.1 km² and average 7.4 km² (Table S1 in Supporting Information S1). The substrates are either metamorphic or granitic rocks. Riverbeds are typically covered with gravel in the reaches of metamorphic rocks and with sand in the reaches of granitic rocks. While Basins 2–6 intersect with or are very close to the fault, Basin 1 does not cross the fault. Channel width and hillslope angles in Basin 1 are compared to the observations in Basins 2–6 to consider the cause of the transient response observed in Basins 2–6. The trunk stream in Basin 1 continues downstream of the outlet shown in Figure 1 and reaches near the outlet of Basin 2 (Figure S1 in Supporting Information S1). This downstream extension of the trunk stream in Basin 1 is steeper than the upstream section and is possibly affected by the subsidence at the hanging wall of the Yunodake fault (Aoyagi et al., 2021) (Figures S1 and S2 in Supporting Information S1). Therefore, we omitted the downstream extension of Basin 1 and focused on the trunk stream shown in Figure 1, which is less affected by base-level changes due to the Yunodake fault. Basins 2–6 are characterized by steeper downstream reaches and gentler upstream reaches of smaller relief (Figure 1c).

2.2. Channel and Hillslope Morphology

2.2.1. Channel Slope

In a stream at steady state, local channel slope (S) is a function of flow discharge, which is commonly substituted by upstream drainage area (A):

$$S = k_s A^{-\theta} \quad (1)$$

where k_s is a steepness index and θ is a concavity index (e.g., Flint, 1974; Snyder et al., 2000). Equation 1 holds only above a critical drainage area ($A > A_{\text{crit}}$), at which the dominant erosional process changes from colluvial (debris flows) to fluvial processes (e.g., Montgomery & Foufoula-Georgiou, 1993; Stock & Dietrich, 2003). The standard stream power model (e.g., Howard & Kerby, 1983) predicts a relation between channel slope and upstream drainage area similar to Equation 1:

$$S = (E/K)^{1/n} A^{-m/n} \quad (2)$$

where E is a local erosion rate, K is erodibility, m is related to the dominant erosion process and hydraulic scaling relationships among channel width, flow discharge, and drainage area, and n is related to the dominant erosion process (e.g., Whipple & Tucker, 1999). From Equations 1 and 2, under a steady state where local erosion rates match local uplift rates (U), channel steepness can be written as

$$k_s = (E/K)^{1/n} = (U/K)^{1/n} \quad (3)$$

Because the concavity index is independent of uplift rates when the gradient of local uplift rates within a basin has a negligible impact on a channel profile (e.g., Snyder et al., 2000), a fixed concavity index ($\theta = \theta_{\text{ref}}$, Equation 1) is used to calculate k_s , and the resulting channel steepness is termed a normalized steepness index (k_{sn} ; Wobus et al., 2006). Assuming a spatially uniform E and K , integrating Equation 1 with respect to the upstream distance along a stream course (x) yields:

$$z(x) = z(x_b) + k_s A_0^{-\theta} \chi \quad (4)$$

$$\chi = \int_{x_b}^x (A_0/A(x))^\theta dx \quad (5)$$

where x_b is the distance at the outlet (thus $x_b = 0$) and A_0 is reference drainage area which was set to 1 m² in this study. Equation 4 predicts that the slope of a χ -plot represents a reach-averaged value of k_{sn} (Perron & Royden, 2013).

A sustained increase in the rate of base-level lowering can generate a knickpoint or a knickzone (e.g., Whittaker & Boulton, 2012). This knickpoint travels upstream and separates the longitudinal river profile into two segments: an adjusted segment downstream with higher steepness and a pre-adjusted segment upstream with lower steepness. When $n < 1$ and rates of base-level lowering increase, or $n > 1$ and rates of base-level lowering decrease, a knickzone is formed between the upstream gentler river segments and downstream steeper segment (Royden & Perron, 2013). Channel steepness in the knickzone gradually increases from the value at an older steady state to the value at a newer steady state. In this case, we define the upstream end of the knickzone as a knickpoint. This type of knickpoint, called a slope-break knickpoint (e.g., Whipple et al., 2013), is readily distinguished from a vertical-step knickpoint that has different origins, such as a local decrease in bed erodibility associated with resistant substrates.

2.2.2. Channel Width

The channel width (W) of bedrock rivers can be a power function of drainage area (e.g., Montgomery & Gran, 2001), a surrogate for upstream drainage area:

$$W = k_w A^b \quad (6)$$

where k_w (unit: m^{1-2b}) is a wideness index (e.g., Allen et al., 2013) and b is a positive exponent that is typically 0.3–0.5 at a steady state (e.g., Whipple, 2004). A larger wideness index indicates a wider channel. Similar to k_{sn} and θ_{ref} , k_w calculated using a fixed value of b (b_{ref}) is a normalized wideness index (k_{wn}). An adjustment in channel width in response to accelerated incision should appear as a break in the hydraulic scaling of Equation 6 or a change in average k_{wn} values with distance along the stream. When uplift rates are spatially variable, channel width does not necessarily follow Equation 6 even after the knickpoint passage and is adjusted for local incision rates to match local uplift rates (e.g., Amos & Burbank, 2007; Lavé & Avouac, 2001; Whittaker et al., 2007).

2.2.3. Angle of Valley-Side Slopes

In mountainous landscapes, drainage basins consist primarily of hillslopes, and material transport on hillslopes dictates the sediment supply to channels (e.g., Roering, 2008). Following the passage of a knickpoint produced by increased base-level-lowering rates, hillslopes become steeper such that hillslope lowering keeps pace with channel incision (e.g., Roering et al., 2001). A downstream increase in hillslope angle is expected downstream of a slope-break knickpoint, and our analysis focused on this transition. Channel width adjustments following the passage of the knickpoint can influence adjacent hillslopes (e.g., Baynes et al., 2022). We considered the influence of width adjustment in discussion.

2.3. Knickpoint Travel Time

Following a sustained increase in incision rates, knickpoint travel distance in χ -space when $n < 1$ is written as (Mitchell & Yanites, 2019; Royden & Perron, 2013):

$$\chi_{\text{kp}}(t) = \frac{nU_{\text{ini}}}{\left(\frac{U_{\text{ini}}}{K}\right)^{\frac{1}{n}} A_0^{-\frac{m}{n}}} t \quad (7)$$

where $\chi_{kp}(t)$ is a χ of a mobile knickpoint at time t since knickpoint generation. We used n values of 0.42 and 2/3, which we will explain in the later section. A_0 is 1 m² in this study. Subscript ini represents the initial steady state; thus U_{ini} is an initial uplift rates. Substituting Equation 3 for Equation 7 and solving Equation 7 with respect to t , the knickpoint travel time since the incision rate increase ($t = 0$) is

$$t = \frac{k_{sn\,ini}}{nU_{ini}} \chi_{kp}(t) \quad (8)$$

2.4. Basin-Averaged Erosion Rate Determined From Cosmogenic ¹⁰Be Concentration

The ¹⁰Be concentration in fluvial sediment (\bar{C} : atoms/g) is used to estimate the average erosion rate within a catchment (\bar{D} : g/m² yr) (e.g., Bierman & Steig, 1996; Brown, Stallard, et al., 1995; Granger et al., 1996) by

$$\bar{D} = P_0 \Lambda / \bar{C} \quad (9)$$

where P_0 (atoms/g yr) is the cosmogenic ¹⁰Be production rate at the surface and Λ (g/cm²) is the attenuation length of particles responsible for ¹⁰Be production. Because the total sediment mass produced in a catchment is the sum of the sediment from its nested sub-catchments, average erosion rates within and outside the sub-catchments can be estimated by analyzing ¹⁰Be samples from multiple sites in the catchment (e.g., Regalla et al., 2013):

$$\bar{D} = \sum_{i=1}^j D_i A_i / \sum_{i=1}^j A_i \quad (10)$$

where D_i and A_i are the average erosion rate and drainage area of sub-catchment i , respectively, and j is the number of subcatchments.

3. Method

3.1. Observations of Channel and Hillslope Morphology

We compiled observations of the along-trunk variations of channel slope, channel width, and hillslope angle as detailed below. We used the channel slope data to identify the current knickpoint position, and we used the other observations to examine the transient response of channel width and hillslope angles and determine the points where the adjustments of channel width and hillslope angle started and finished.

3.1.1. Normalized Steepness Index

We analyzed a digital elevation model (DEM) of the study area to calculate the normalized steepness index k_{sn} every 50 m along trunk streams using Topotoolbox 2 (Schwanghart & Scherler, 2014). The DEM, obtained from the Geospatial Information Authority of Japan, has a resolution of 10 m. We first determined A_{crit} using log-log plots of channel slope and drainage area and then calculated k_{sn} for channel reaches with $A > A_{crit}$. We used θ_{ref} of 0.45, which were close to the average θ value for the trunk streams analyzed (Table S1 in Supporting Information S1) and commonly used in calculating k_{sn} . We also calculated χ and constructed χ -elevation (z) plots (χ -plots). We used the k_{sn} values and χ -plots to determine the current positions of slope-break knickpoints (at the upstream end of knickzones), where the adjustment of channel slope begins.

3.1.2. Field Measurement of Channel Width

We measured bankfull channel widths in the field every 30–100 m along trunk streams using a laser rangefinder (TruPulse 360B, Laser Technology). Measurement error is approximately ± 30 cm. Width measurements depend on how one defines flow depth at bankfull stage. The bankfull depth is typically identified based on the limits of active abrasion, vegetation boundaries, and remnants of flood debris (e.g., Whittaker et al., 2007). Where there were multiple candidates for the high-flow depth, we measured channel widths at each candidate level and calculated their average. Equation 6 was fit to the measured width of each trunk river to estimate exponent b based on least squares. We determined b_{ref} by averaging b of all river segments whose width variations were consistent with the general scaling of Equation 6. We then used the resulting b_{ref} values and upstream drainage areas calculated from the 10 m DEM to calculate the normalized wideness index k_{wn} .

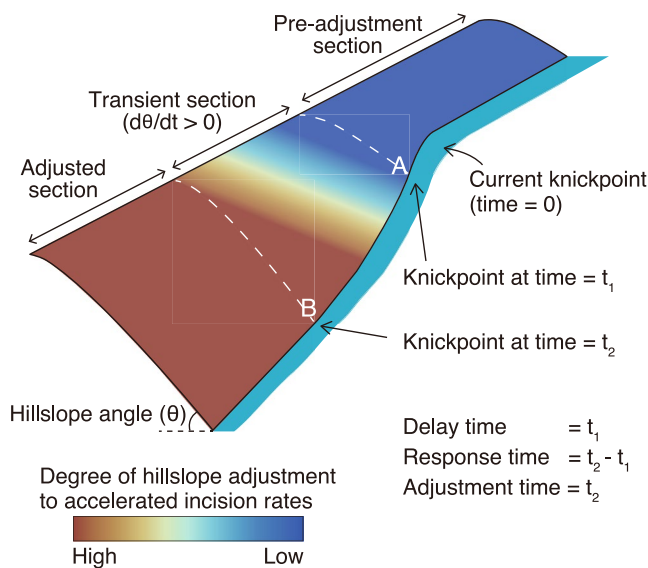


Figure 2. Schematic diagram of the right bank of a stream showing the response of the hillslope angle to accelerated incision. The hillslope angle starts to change at the boundary between the pre-adjustment and transient sections (site A) and finishes at the boundary between the transient and adjusted sections (site B).

3.1.3. Average Angle of Valley-Side Slopes

We calculated the angles of hillslopes adjacent to trunk streams using the 5 m DEM provided by the Geospatial Information Authority of Japan. We used this high-resolution DEM because the accuracy of hillslope angles depends on the DEM grid size. Because the available 5 m DEM lacks data along the streams, we could not use it for the channel analysis. We mapped hillslopes along trunk streams based on the upstream drainage area, slope aspect, and slope curvature. We did not include hillslopes along tributaries with drainage areas greater than A_{crit} as our focus was on trunk streams. Although it was difficult to determine a clear threshold, we also excluded hillslopes along small tributaries (maximum area $< A_{\text{crit}}$) visible on the 5 m DEM (Figure S3 in Supporting Information S1). We then segmented mapped valley-side slopes every 50 m along trunk streams and calculated average angles for each hillslope segment.

3.1.4. Identifying Sections of Transient Response

To identify river sections where hillslopes and channels are undergoing a transient response to accelerated incision, we used an R (R Core Team, 2022) package mcp, a Markov chain Monte Carlo algorithm for Bayesian regression with change points (Lindeløv, 2020). The algorithm searches for regression models and the positions of the change points that best explain the variation of k_{wn} and hillslope angle. We followed the default settings except for the regression models, the number of change points, and the prior distributions.

Graphical representations of the procedures and input parameter values are presented in the Supporting Information S1 (Figure S4 and Table S2). We modeled the variations of k_{wn} and hillslope angle using two horizontal lines connected by a slant line (Figure S4a in Supporting Information S1). The intersections of the horizontal and slant lines are the change points and correspond with the downstream and upstream ends of the section in transience (a transient section in Figure 2). We ran three chains and obtained $3 \times 3,000$ realizations for the change point positions. A Gelman-Rubin diagnostic for the positions of change points was 1.0 for all the runs, indicating that the models converged well (Gelman & Rubin, 1992). To determine the uncertainty of the positions of the change points, we stacked histograms of the three chains (Figure S4b in Supporting Information S1). We then picked up bins with greater probability until the cumulative probability of the selected bins reached 68% (Figure S4c in Supporting Information S1). The minimum and maximum values of the selected bins were used as the downstream and upstream bounds of the change point positions. As a result, the uncertainty ranges of the change point positions for k_{wn} and hillslope angles cover 68%–91% and 68%–93% of the 9,000 realizations, respectively.

3.2. Adjustment Timescales of Channel Width and Hillslope Angle

Figure 2 schematically illustrates the response of a valley-side slope to accelerated incision, which is characterized by three sections representing the different phases of morphological adjustment to increased incision rates (e.g., Hurst et al., 2012). The response of channel width and its impact on hillslope angle (e.g., Baynes et al., 2022) is omitted from Figure 2 for simplicity. The pre-adjustment section extends from upstream to downstream of the knickpoint and reflects the incision rate before acceleration. Downstream of the pre-adjustment section is the transient section where width or hillslope angles are changing from an older steady state value to a new steady state value. The most downstream section is the adjusted section that is already adjusted to the accelerated incision. The delay time is the knickpoint travel time from the boundary between the pre-adjustment and transient sections (site A in Figure 2) to the current knickpoint position. The knickpoint travel time from this boundary (site A in Figure 2) to the boundary between the transient and adjusted sections (site B in Figure 2) is the response time. The adjustment time is the sum of the response and delay times or knickpoint travel time from the boundary between the transient and adjusted sections (site B in Figure 2) to the current knickpoint position.

Using Equation 8 and assuming that one step increase in incision rates produced knickpoints at the intersections of the stream and the Yunodake fault, we first calculated knickpoint travel time and then calculated elapsed time

since the knickpoint passage. We use the elapsed time because we need to know the position of the knickpoint at a specific time in the past rather than the total travel time from its origin to each point on trunk streams. We used n values of 0.42 and 2/3. The n value of 0.42 was obtained by fitting Equation 3 to the results of average k_{sn} and erosion rates. We also used $n = 2/3$ because it is commonly used (e.g., Whipple et al., 2000) and is within the 95% confidence intervals of our n estimate (0.10–0.74). The m values (Equation 2) were calculated assuming $m/n = \theta_{ref}$. The choice of m affects only the unit of the erodibility coefficient and does not influence the result. Normalized channel steepness at the initial steady state were assumed to be the average k_{sn} upstream of a slope-break knickpoint.

We assumed that the erodibility constant (K) was uniform over time and calculated K using k_{sn} and ^{10}Be -derived erosion rates with Equation 3. We used our results of ^{10}Be analysis and those previously reported in the Abukuma massif (Table S3 in Supporting Information S1; Regalla et al., 2013; Nakamura et al., 2014; Matsushi et al., 2014). The Abukuma massif is located at the north of Iwaki, and the sampled catchments in the Abukuma massif mainly consist of similar granitic rocks to those in Iwaki (Kubo & Yamamoto, 1990). Results of ^{10}Be -analysis and k_{sn} values in Abukuma massif were recalculated using the same methods we used in Iwaki. The uncertainty range of K in Iwaki and Abukuma massif overlaps with each other (Table S4 in Supporting Information S1). Therefore, we first calculated K using individual sets of mean k_{sn} and ^{10}Be -derived erosion rates obtained in Iwaki and Abukuma massif and then calculated their mean and standard deviation, which were used to calculate knickpoint travel time and its uncertainty. The uncertainty in K for metamorphic rocks was calculated using a standard deviation of k_{sn} and an error of ^{10}Be -derived erosion rates, because only one sample was taken from a catchment dominated by metamorphic rocks.

The erodibility coefficient K probably changes through time primarily due to the variations in climate conditions (e.g., Petit et al., 2017). However, Goren (2016) revealed that uplift histories inferred from river long profiles were similar between the cases using constant K and temporally variable K with a period of $\sim 10^5$ years. This finding suggests it is reasonable to assume that the variations of K due to climate change, such as Milankovitch cycles, is minimum. We note that other factors, such as the changes in substrate lithology during incision and weathering speed, may also cause the temporal variation of K , which adds additional uncertainties in the estimates of knickpoint travel time and adjustment timescale of width and hillslope angles.

Based on the change point positions inferred from the Bayesian analysis and the elapsed time since knickpoint passage, we estimated the delay, response, and adjustment times of channel width and hillslope angles in response to a sustained increase in incision rates. Uncertainties for the three timescales were associated with the inferred change point positions and the erodibility K .

3.3. Basin-Averaged Erosion Rate Determined From Cosmogenic ^{10}Be Concentration

We collected four sand samples (diameter < 2 mm) from trunk streams and measured ^{10}Be concentrations of quartz grains to determine basin-averaged erosion rates (Figure 1). We purified quartz following a method adapted from Kohl and Nishiizumi (1992). We first crushed and sieved samples to obtain grains 0.25–1 mm in diameter. These were heated in 9% HCl to remove carbonates, iron oxides, and organic materials, then quartz was separated from the samples using sodium polytungstate. The extracted quartz was leached using a 1% HF and HNO_3 solution to remove residual feldspars and meteoric ^{10}Be . Then, after adding a ^9Be spike, the quartz was dissolved with HF, HNO_3 , and HClO_4 . After the solution was used in anion- and cation-exchange chromatography, NH_4OH was added, and the precipitant was heated to obtain BeO . $^{10}\text{Be}/^9\text{Be}$ ratios were measured using accelerator mass spectrometry at Micro Analysis Laboratory, Tandem Accelerator, the University of Tokyo (Matsuzaki et al., 2007).

^{10}Be production rates were calculated using scaling factors presented in Stone (2000). We computed topographic shielding factors for all sampled points using the 10 m DEM and an algorithm developed by Li (2013). Attenuation lengths for neutrons, slow muons and fast muons were set at 160, 1,500, and 5,300 g/cm², respectively (Braucher et al., 2003; Brown, Bourlès, et al., 1995; Gosse & Phillips, 2001). Contributions of slow and fast muons to the total ^{10}Be production at the surface were assumed to be 1.2% and 0.65%, respectively (Braucher et al., 2003). We assumed a bulk density of 1.63 g/cm³ for the shallow subsurface materials on hillslopes (Nakamura et al., 2014). Although it sometimes snows in Iwaki, we did not consider the effect of snow shielding on ^{10}Be production because the snow cover was mostly less than several centimeters deep during 1960–2008 (Japan Meteorological Agency, 2021).

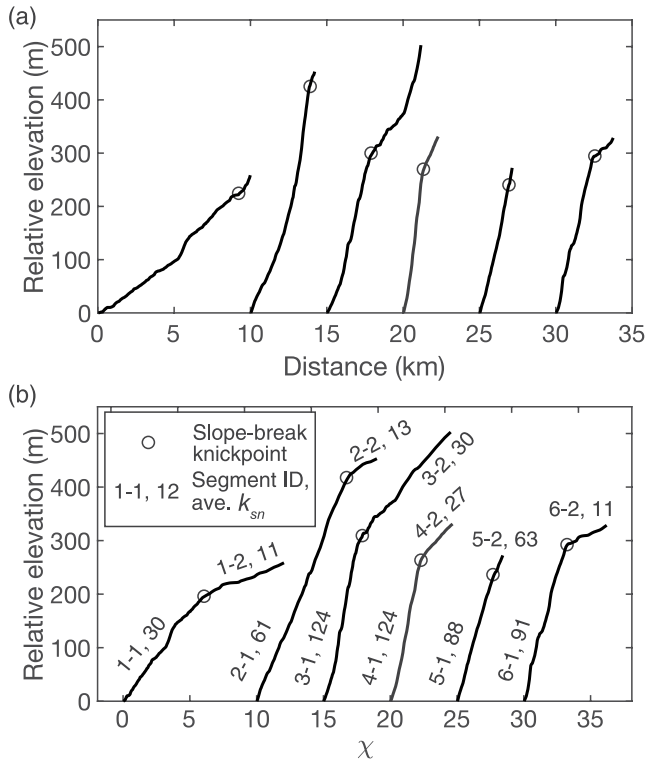


Figure 3. (a) Longitudinal profiles and (b) χ -plots for the trunk streams in Basins 1 to 6. Relative elevation (y-axis) denotes the elevation above the basin outlet.

4. Results

4.1. Channel and Hillslope Morphology

4.1.1. Steepness of Stream Channels

Calculated values of normalized channel steepness (k_{sn}) are summarized in Figure 3. Each of the six drainage basins contains a slope-break knickpoint dividing the trunk streams into a downstream segment with greater k_{sn} and an upstream segment with smaller k_{sn} (Figures 1 and 3). Downstream segments of Basins 2–6 are steeper than that of Basin 1, suggesting that incision rates in Basin 1 are slower than in other basins. The channel steepness in the downstream segment of Basin 1 is three times greater than that of the upstream segment (Figure 3), which is probably related to non-tectonic factors (Figures S1 and S2 in Supporting Information S1). A slope-break knickpoint in Basin 3 occurs near a boundary between granitic rocks and schist (Figure 1), presenting the possibility that differential rock erodibility may explain the observed increase in k_{sn} . However, channel steepness does not change significantly at similar lithologic boundaries in Basins 3 and 4 (Figure 1b). Therefore, we assumed that factors other than differential rock erodibility contributed to the formation of the knickpoint in Basin 3.

4.1.2. Channel Width

We measured channel width and depth at 308 points, which are presented in the Supporting Information S1 (Table S5 in Supporting Information S1). The normalized widthness index (k_{wn} , $b_{ref} = 0.42$) is shown against the distance from the outlet in Figure 4. Plots of width-drainage area are shown in Figure S5 in Supporting Information S1. We also calculated k_{wn} using the exponent b_{ref} estimated from data in each basin (Table 1) and confirmed the results were similar to those calculated from uniform b_{ref} (Figure S6 in Supporting Information S1). In Basins 1, 2, and 4, k_{wn} did not change significantly over

their entire reaches (Figures 4a, 4b, and 4d). k_{wn} for the trunk streams of Basins 1 and 2 are identical despite their twofold difference in k_{sn} (Table 1). This result implies that their channel widths are insensitive to changes in channel incision rates (e.g., Snyder et al., 2003; Zhang et al., 2017) or possibly have not started to adjust to the accelerated incision. In contrast, k_{wn} in Basins 3 and 5 were different between their upstream and downstream reaches (Figures 4c and 4e). At the distance of ~ 2.5 km in Basin 3, k_{wn} decreases downstream. This transition occurs near the lithologic boundary between granitoids and schist (Figure 4c). In Basin 5, although k_{wn} decreases downstream at a distance of ~ 1 km, the difference in average k_{wn} between reaches upstream and downstream of the knickpoint is small compared to the variation in Basin 3.

There is also a clear variation of k_{wn} in Basin 6; however, unlike in Basins 3 and 5, k_{wn} does not simply decrease downstream. k_{wn} is around $10 \times 10^{-3} \text{ m}^{0.16}$ in the very upstream section (distance > 3 km) and suddenly increases to $14\text{--}21 \times 10^{-3} \text{ m}^{0.16}$ around the knickpoint and then decreases to $6 \times 10^{-3} \text{ m}^{0.16}$ at a distance of 1 km (Figure 4f). The small k_{wn} upstream of the knickpoint probably resulted from recent human activity. Aerial photographs taken in 1976 and 1986 show that many trees at the headwaters of Basin 6 were cut during this period, and the surrounding areas were widely excavated (Figure S7 in Supporting Information S1). This human activity displaced large amounts of soil, which currently occupies the channel and results in channel narrowing upstream of the knickpoint. While bedrock is hardly exposed at the channel walls and bed upstream of the knickpoint, bedrock outcrops extensively downstream of the knickpoint.

4.1.3. Angle of Valley-Side Slopes

As illustrated in Figure 2, hillslopes in Basins 1–6 consist of three sections: an upstream section with gentler slopes, a downstream section with steeper slopes, and an intervening transient section. Hillslope angles in the upstream sections were positively correlated with normalized channel steepness (Figure 5a). In the downstream sections, hillslope angles were less sensitive to channel steepness and clustered at $35^{\circ}\text{--}38^{\circ}$, suggesting that these are predominantly threshold hillslopes (e.g., Ouimet et al., 2009). Left-skewed distributions of hillslope angles

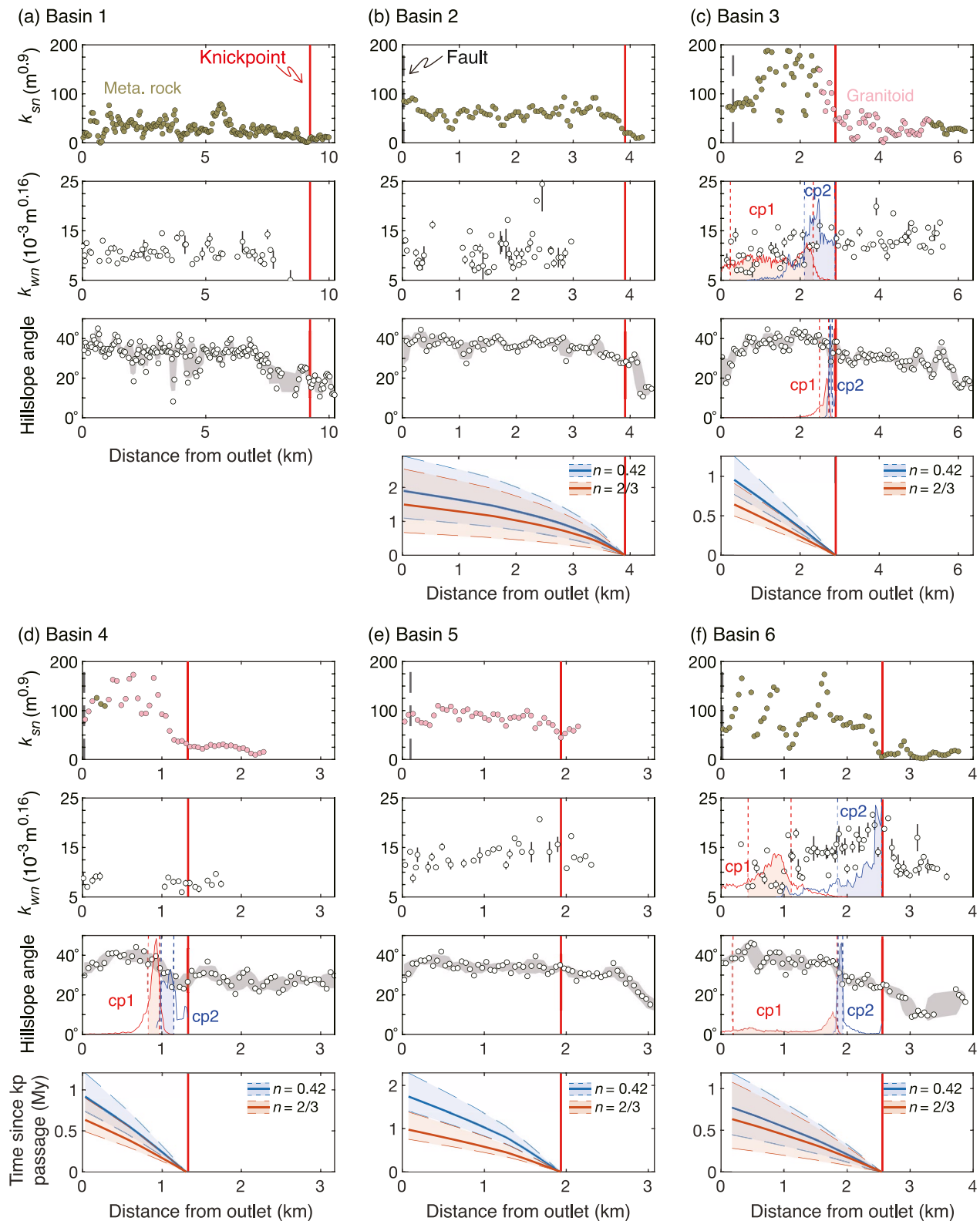


Figure 4.

Table 1
Results of Field Measurement and Regression of Channel Width

Basin/segment	Max. area (km ²)	Min. area (km ²)	k_w	b^a	R^2	Ave k_{wn} (10 ⁻³ m ^{0.16})
1	24.1	0.025	3.45	<i>0.43</i>	0.73	10.6
2	4.6	0.021	3.43	<i>0.40</i>	0.41	10.2
3	6.9	0.021	5.37	0.20	0.20	12.0
3-downstream	6.9	6.2	2.52	0.52	0.03	9.2
3-upstream	5.4	0.021	4.70	<i>0.35</i>	0.51	13.2
4	1.6	0.1	2.69	<i>0.52</i>	0.73	8.1
5	3.4	0.4	4.75	0.30	0.64	13.4
5-downstream	3.4	2.8	5.28	0.18	0.00	12.1
5-upstream	2.4	0.4	4.79	<i>0.39</i>	0.65	14.3
6	3.8	0.3	4.73	0.26	0.13	12.8
6-downstream	3.8	1.7	7.19	-0.17	0.03	12.6
6-upstream	1.6	0.3	2.96	1.77	0.53	12.7

^aNumbers in italics were used to calculate b_{ref} .

also support the interpretation that the downstream sections have threshold hillslopes (Figure 5b) (DiBiase et al., 2012). The histograms for hillslope angles along the trunk stream distinctly differ from those for the whole basin (Figures 5b and 5c). This difference is apparent even in Basin 2, where the slope-break knickpoint is located near the channel head, indicating the lagged response of hillslope angles along the tributaries following an increase in incision rates of the trunk stream.

4.1.4. Identifying Sections Undergoing Transient Response

We performed the change point analysis for k_{wn} (Basins 3 and 6) and hillslope angle (Basins 3, 4, and 6). We excluded k_{wn} in Basin 5 because k_{wn} upstream of the knickpoint in Basin 5 is not very different from those downstream of the knickpoint. We also excluded the hillslope angles of Basins 2 and 5 from the analysis. This is because the data points upstream of the knickpoint were limited in Basin 2 and the downstream increase in hillslope angles was unclear compared to other basins. The inferred positions of the two change points are shown in the second and third panels of Figures 4c, 4d, and 4f. The downstream and upstream change points cp1 and cp2 represent the downstream and upstream ends of the transient section. The uncertainty ranges are shown below the frequency curves. Most curves have irregular shapes and are not unimodal, indicating that the precise identification of the change points is challenging. The uncertainty ranges are wider for k_{wn} than

for hillslope angles. The downstream change point cp1 for k_{wn} are found farther downstream of cp1 for hillslope angles (Figure 4c), indicating channel width and hillslope angles have different adjustment times.

The uncertainty ranges of the cp1 position for hillslope angles extend downstream, suggesting the gradual increase in hillslope angles may occur after the large increase in hillslope angles at the initial stage of the adjustment (Figures 4c, 4d, and 4f). Although the left-skewed frequency curves for cp1 result partly from the model constraint that cp1 occurs downstream of cp2, the hillslope angles slightly increase downstream by several degrees within the negative tails of the frequency curves (Figures 4c, 4d, and 4f). The gradual increase is observed even in Basin 5. Although Basin 5 lacks evidence of significant hillslope steepening, the hillslope angles increase from 30°–35° at a distance of ~1.8 km to 33°–37° at a distance of ~0.5 km (Figure 4e).

4.2. Adjustment Timescales Calculated From Knickpoint Travel Times

4.2.1. Substrate Erodibility Calculated From Basin-Averaged Erosion Rates

The basin-averaged erosion rates of our study basins ranged between 260 and 400 g/m²/yr, equivalent to 0.16–0.25 mm/yr (Table 2). Basin 4 differs from the others in consisting almost entirely of granitic rock. It also lacks evidence of recent large slope failures, which dilute the average ¹⁰Be concentration of fluvial sand downstream by supplying material with low ¹⁰Be concentrations. Thus, we used Equation 10 to calculate the basin-averaged erosion rate of the downstream half of the Basin 4 (IWK4-1, Table 2; Figure S8 in Supporting Information S1). The downstream erosion rate is faster than that of the upstream half of Basin 4 (IWK4-2, Table 2; Figure S8 in Supporting Information S1). Overall, basin-averaged erosion rates were positively correlated with average k_{sn} (Table 2; Figure S9 in Supporting Information S1). Therefore, we assume that the erosion rates determined from the ¹⁰Be concentrations reflect channel incision rates and can be used to calculate the erodibility K in Equation 2.

We then estimated a slope exponent n by fitting Equation 3 to average k_{sn} and the basin averaged erosion rates in Iwaki and the Abukuma massif (Figures S8 and S10 in Supporting Information S1). The estimated n is 0.42 and

Figure 4. Variations of channel width and hillslope angles along the trunk stream in Basins 1–6. In figures (a–f), the top panel shows k_{sn} and substrate rock types, the second panel shows normalized wideness (k_{wn}), the third panel shows average hillslope angles in each 50 m segment of the trunk stream, and the bottom panel shows the elapsed time since knickpoint (kp) passage for $n = 0.42$ and $2/3$. The elapsed time represents the time when the knickpoint passed that position and is calculated from the knickpoint travel time (Equation 8). The gray area in the third panel indicates a 5-point moving average and standard deviation. (b–f) In the second and the third panels, red and blue lines indicate the probability distributions for the change point positions, and the red and blue areas bounded by the vertical broken lines indicate the ranges of the change point positions used to calculate the adjustment timescales (see Section 3.1.4. for the details).

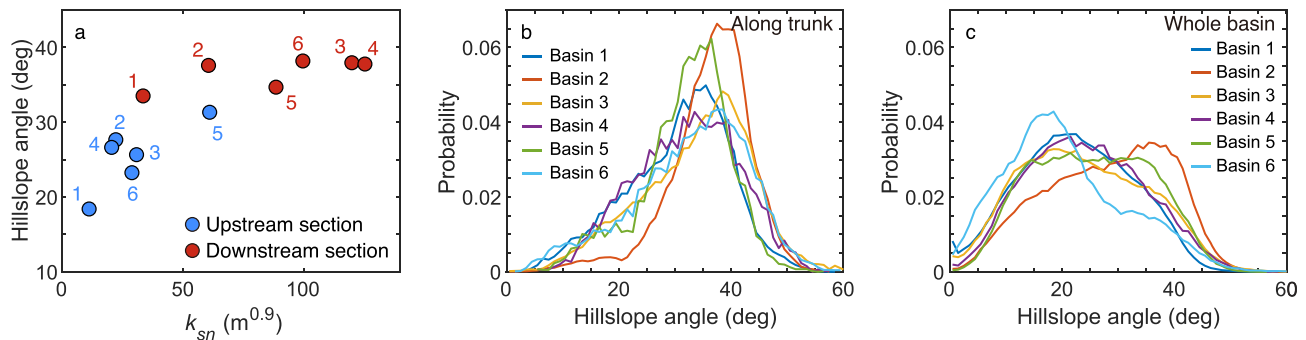


Figure 5. (a) Hillslope angle versus normalized channel steepness for upstream and downstream segments of the six basins. (b) Histogram of hillslope angles along trunk streams. (c) Histogram of hillslope angles in each entire basin. The bin widths in (b) and (c) are 1° .

ranged from 0.10 to 0.74 (95% confidence interval). These estimates are smaller than the global average (Harel et al., 2016); however, $n < 1$ is possible at slower erosion rates (Figure 5 in Harel et al., 2016; Hilley et al., 2019). The smaller n in the confidence bounds results in inconsistent knickpoint travel time among the studied basins. Therefore, we used the n value of 0.42 and the commonly used value of $2/3$ (Whipple et al., 2000).

Using k_{sn} and basin-averaged erosion rates, we determined the erodibility coefficient K for granitic and metamorphic rocks. The coefficient K for granitic rocks were $4.2 \pm 1.0 \times 10^{-5} m^{0.595}/yr$ ($n = 0.42$) and $1.7 \pm 0.5 \times 10^{-5} m^{0.4}/yr$ ($n = 2/3$). The coefficients for metamorphic rocks were $2.6\text{--}6.9 \times 10^{-5} m^{0.595}/yr$ ($n = 0.42$) and $1.0\text{--}3.8 \times 10^{-5} m^{0.4}/yr$ ($n = 2/3$). Although the uncertainty in K for metamorphic rocks is large, the similarity of K between granitic and metamorphic rocks is consistent with the fact that the reaches of granitic and metamorphic rocks have comparable channel steepness (Figure 1b).

4.2.2. Knickpoint Travel Time

We estimated knickpoint travel time using the uplift (erosion) rates at the initial steady states, erodibility coefficients, and a slope exponent n (Equation 8). Parameters used to calculate travel time and the results are shown in Table 3. The travel times in Basin 2 and 5 were longer than those in other basins when $n = 0.42$ (Table 3). When $n = 2/3$, the estimated travel times for the basins 2–6 overlapped with each other at $\sim 0.8\text{--}0.9$ My.

In order to validate the knickpoint travel time estimated from Equation 8, we also calculated the travel time by reconstructing a paleo-longitudinal profile that was adjusted to the pre-accelerated incision rates in Basin 4 (Figure 6). The elevation difference between the reconstructed and the present profile (Figure 6) is 206 m. The difference in basin averaged erosion rates between the upstream and the downstream section of Basin 4 (Figure 6) is 0.41 mm/yr at a maximum. The minimum difference in the incision rates could not be obtained because the

Table 2
Basin-Averaged Erosion Rates Determined From ^{10}Be Concentrations

Sample ID	Mass sample (g)	Mass ^{9}Be carrier (g)	$^{10}Be/^{9}Be$ ($\times 10^{-14}$) ^a	^{10}Be concentration (atoms/g)	^{10}Be production rate (atoms/g yr) ^b	Erosion rate (g/m ² /yr)	Erosion rate (mm/yr) ^c	Upstream ave. k_{sn} ($m^{0.9}$) ^d
IWK1	26.4364	3.4882	7.5 ± 0.51	$55,627 \pm 4,929$	7.0 ± 0.4	261 ± 37	0.16 ± 0.03	28
IWK4	39.3525	2.4981	17.5 ± 2.2	$67,402 \pm 9,578$	6.6 ± 0.4	391 ± 63	0.24 ± 0.04	59
IWK3	39.4954	2.4994	10 ± 0.90	$34,884 \pm 4,041$	7.2 ± 0.4	405 ± 62	0.25 ± 0.04	25
IWK4-2	40.0002	2.4809	10.6 ± 0.88	$36,878 \pm 3,920$	6.9 ± 0.4	329 ± 46	0.20 ± 0.03	17
IWK4-1*						598 ± 396	0.37 ± 0.24	120

Note. * Average rate for the downstream sub-catchment of Basin 4 calculated from Equation 10.

^aResults based on the KNB5-1 ^{10}Be standard (Nishiizumi et al., 2007). The $^{10}Be/^{9}Be$ ratio for the chemical blank was $1.8 \times 10^{-14} \pm 0.30 \times 10^{-14}$. ^bWe used the production rate at sea level and a high latitude of $4.68 \text{ atoms g}^{-1} \text{ yr}^{-1}$, corrected from the value proposed by Stone (2000), assuming a ^{10}Be half-life of 1.387 My (Chmeleff et al., 2010; Korschinck et al., 2010). ^cThe bulk density of the samples was 1.63 g/cm^3 (Nakamura et al., 2014). ^dAverage k_{sn} for trunk and tributaries upstream from a sampling point.

Table 3
Parameters and Results of the Calculation of Knickpoint (kp) Travel Time

Basin	$k_{sn\ ini}$	$U_{ini}, n = 0.42$ (mm/yr)	$U_{ini}, n = 2/3$ (mm/yr)	kp travel distance (km)	kp travel distance (χ)	kp travel time $n = 0.42$ (My)	kp travel time $n = 2/3$ (My)
2	13	0.12 (0.08–0.2)	0.09 (0.06–0.21)	3.9	7.2	1.9 (1.1–2.9)	1.5 (0.7–2.5)
3	30	0.18 (0.13–0.22)	0.16 (0.12–0.21)	2.6	2.4	1.0 (0.8–1.3)	0.6 (0.5–0.9)
4	27	0.17 (0.13–0.21)	0.15 (0.11–0.2)	1.1	2.1	0.9 (0.7–1.2)	0.6 (0.5–0.9)
5	63	0.24 (0.18–0.3)	0.27 (0.19–0.35)	1.9	2.8	1.8 (1.4–2.3)	1.0 (0.8–1.4)
6	11	0.11 (0.07–0.19)	0.08 (0.05–0.19)	2.4	3.2	0.8 (0.5–1.2)	0.6 (0.3–1.1)

estimates on incision rates before and after acceleration overlap with each other (IWK4-1 and 4-2, Table 2). Dividing the elevation difference by the difference in incision rates yields a minimum knickpoint travel time of 0.5 My, consistent with the travel time estimated from Equation 8.

4.2.3. Adjustment Timescales

The three timescales (response, delay, and adjustment times) for the cases of $n = 0.42$ and $n = 2/3$ are presented in Figure 7. Due to the large uncertainties, it is difficult to quantitatively compare results for channel width with those for hillslope angle. Nevertheless, in Basin 3, the response, delay, and adjustment times are probably longer for channel width than hillslope angles. Adjustments of width and hillslope angles take comparable times in Basin 6. These results from the large uncertainty in the change point position of hillslope angles associated with the gradual hillslope steepening (Figure 4f). The uncertainty range of cp1 for hillslope angles in Basin 6 covers 93% of the model output, greater than the coverages in other basins (68%–72%). Indeed, the adjustment time calculated from the mode value of the cp1 position (distance ~ 1.8 km) is less than 0.5 My (Figure S11 in Supporting Information S1). Therefore, if the gradual increase in hillslope angle following relatively sudden steepening of the hillslopes is related to the accelerated incision, hillslope adjustment may take a comparably long time with the width adjustment.

5. Discussion

5.1. Cause of Knickpoint Formation

The average erosion rates in Basin 4, which are faster downstream of the slope-break knickpoint than upstream, support the idea that accelerated river incision is responsible for the observed transient behavior. The common occurrence of slope-break knickpoints and the similar knickpoint travel times among Basins 2–6 suggest that the incision rates accelerated at the same time. We attribute the increase in incision rates to the activity of the Yunodake fault because rivers flowing across the fault (Basins 2–6) are steeper than the river in Basin 1, away from the fault and are probably less affected by the fault (Figure 1; Figures S1 and S2 in Supporting Information S1).

Awata and Kakimi (1985) and Awata (1988) estimated the initiation ages of active faulting under the current stress regime in northeastern Japan (Tohoku) based on average slip rates and cumulative displacement. Doke et al. (2012) conducted an extensive literature review, including Awata and Kakimi (1985) and Awata (1988), and found that faults in Tohoku became active after ~ 3.5 Ma. The onset of fault activity migrated from the Japan sea side at 3.4–2.4 Ma to the Pacific side at 0.9–0.5 Ma Doke et al. (2012). Nakajima (2013, 2018) summarized the tectonic evolution of northeastern Japan mainly based on stratigraphic evidence and pointed out that the intense E-W compression started from 3 to 2 Ma. Several hypotheses were presented to explain the cause of the intense compression, which were related to the changes in motion either of the Pacific Plate, the Philippine Sea plate, and the Amurian Plate (Nakajima, 2013, 2018). Our modeled knickpoint travel times

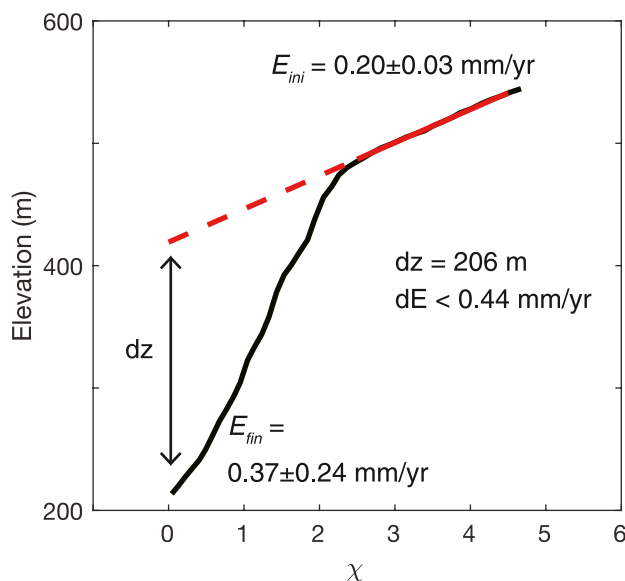


Figure 6. A χ -plot for the trunk stream of Basin 4 and a reconstructed paleo-profile. The red solid line is a regression line fitted to the upstream section of the trunk stream (4-2 in Figure 3), and the red broken line is an extrapolated line of the regression line. dz is the elevation difference between the reconstructed and the present profile. dE is the difference in incision rates between the upstream (E_{ini}) and downstream section (E_{fin}) of Basin 4.

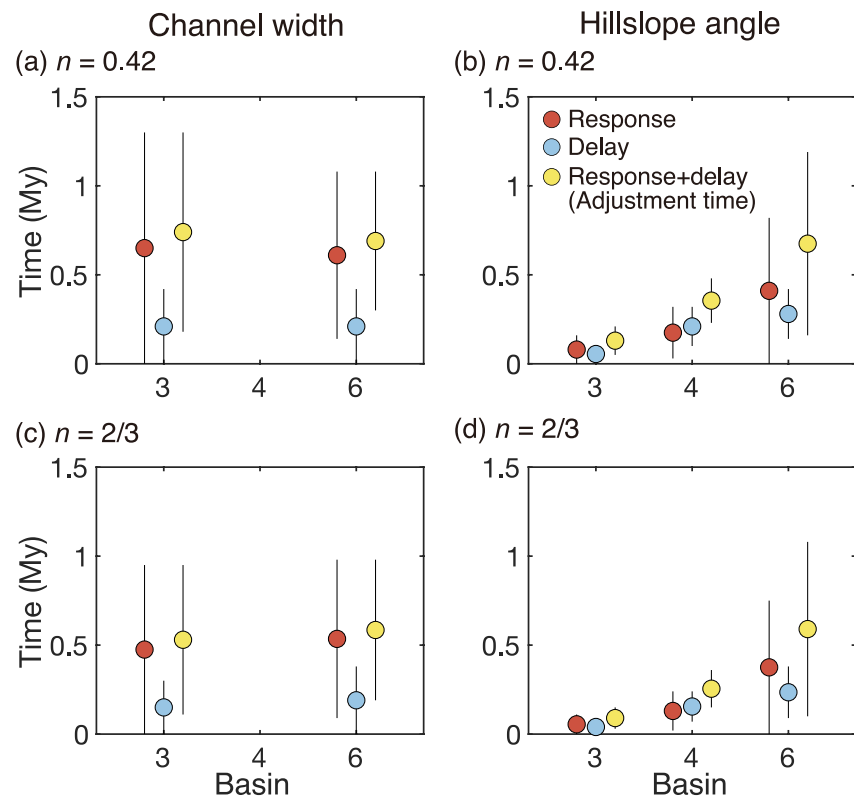


Figure 7. Delay, response, and adjustment times of channel width and hillslope angle in response to an increase in incision rates for the cases of (a, b) $n = 0.42$ and (c, d) $n = 2/3$. The points represent the median values in the uncertainty ranges.

in Basin 2–6 ranged between 0.6 and 1.5 My and overlapped at 0.8–0.9 My when $n = 2/3$ (Table 3), consistent with the inferred onset of fault activity in Tohoku. Therefore, although there is no direct evidence of the throw rate of the Yunodake fault increasing during the middle Pleistocene, we attribute the generation of slope-break knickpoints to changes in throw rates of the fault.

5.2. Implications for Transient Response

Our results showed that the transient behavior of width and hillslope angles are quite diverse even when the substrate rock types (metamorphic rock: Basins 2 and 6; granitoid: Basins 3–5) and the histories of base-level changes are similar. The interpretation of k_{wn} is not straightforward due to its natural variability and local factors. In Basin 3, the reduction of k_{wn} occurs near the transition of bedrock from granitoid to schist (Figure 4c). The average k_{wn} values before width adjustment (i.e., k_{wn} in Basins 1, 2, 4, and the upstream section of Basins 3 and 5, Table 1) is $13.1 \pm 3.2 \times 10^{-3} \text{ m}^{0.16}$ in reaches of metamorphic rocks and $12.7 \pm 3.9 \times 10^{-3} \text{ m}^{0.16}$ in reaches of granitoids, which are statistically indistinguishable ($p = 0.17$ in Mann-Whitney U test). Therefore, the reduction of k_{wn} in Basin 3 is difficult to explain by the change in lithology alone.

In Basin 6, k_{wn} abruptly increases up to $\sim 20 \times 10^{-3} \text{ m}^{0.16}$ near the knickpoint, anomalously large compared to k_{wn} in other basins (Figure 4). This wider reach is characterized by fully exposed bedrock at the bed. In contrast, upstream of this wider reach, the valley bottom is completely filled by thick soils associated with recent human activity (Figure S7 in Supporting Information S1), and the channel width is probably narrower than the width before valley filling. Therefore, although the mechanism is unclear, the sudden widening near the knickpoint should be associated with human activity. Downstream of the wider reach near the knickpoint, k_{wn} gradually decreases to $\sim 15 \times 10^{-3} \text{ m}^{0.16}$ at the distance of 1.8–2.3 km and drops to $< 10 \times 10^{-3} \text{ m}^{0.16}$ at the distance of 1–1.4 km (Figure 4f). Channel narrowing at the two locations mentioned above does not correspond with lithologic boundaries or transitions between reaches with and without strong human imprints. There are two possible interpretations. The first interpretation is that the upstream narrowing at the distance of 1.8–2.3 km is

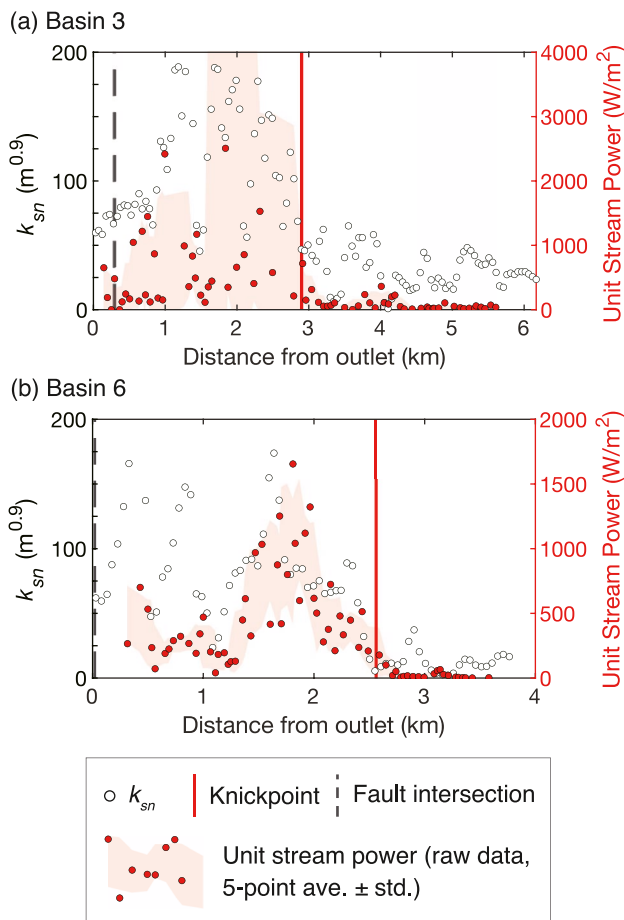


Figure 8. Normalized channel steepness and unit stream power along the trunk streams.

solely associated with human activity (i.e., widening near the knickpoint), and the downstream narrowing at the distance of 1–1.4 km results from the accelerated incision. In this case, the delay time for width adjustment becomes longer than the value in Figure 7; however, the total adjustment time is the same as in Figure 7. The second interpretation is that k_{wn} continues to decrease between 1 and 2.3 km in the distance (Figure 4f). This interpretation is consistent with the change point positions predicted by the change point analysis. Therefore, although it is difficult to decide which interpretation is more plausible, the variation of k_{wn} in Basin 6 cannot be explained without the effects of accelerated incision because the k_{wn} clearly decreases downstream of the knickpoint and becomes smaller than values upstream of the knickpoint.

Spatially heterogeneous rates of base-level changes can also divert channel width from values predicted by Equation 6, which can result in the spatially variable distribution of unit stream power (e.g., Allen et al., 2013; Amos & Burbank, 2007; Whittaker et al., 2007). To test if the channel narrowing observed in Basins 3 and 6 resulted from differential relative uplift by the fault, we calculated unit stream power (ω , W/m^2):

$$\omega = \tau_b V \quad (11)$$

$$\tau_b = \rho g R S \quad (12)$$

$$V = R^{2/3} S^{1/2} / n_M \quad (13)$$

where τ_b is boundary shear stress (Pa), V is flow velocity (m/s), ρ is the density of water ($1,000 \text{ kg/m}^3$), g is the gravitational acceleration (9.8 m/s^2), R is hydraulic radius assuming a rectangular channel (a ratio of a cross-sectional area to wetted perimeter of the flow), n_M is the Manning's roughness coefficient. We estimated n_M by constructing an empirical formula between n_M and channel slope (e.g., Yochum et al., 2014) using an extensive database of flow velocity and channel geometries (Deal, 2021) (Text S1 in Supporting Information S1). We acknowledge the estimated n_M is not very accurate (Figure S12 in Supporting Information S1) because flow stages and bed roughness

heavily impact n_M (e.g., Ferguson et al., 2017; Yochum et al., 2012). Nevertheless, using the empirical formula should help to obtain more realistic estimates of flow velocity than using fixed n_M . The variations of ω along the trunk streams are shown in Figure 8. Unit stream power is greater in reaches downstream of the knickpoint than upstream reaches. The maximum ω does not occur near the fault, and the variation of ω does not depend on the distance from the outlet, suggesting that the spatial variation of uplift rates at the footwall of the fault is minimum and does not have discernible influences on channel width. The vertical displacement during the earthquake in 2011 occurred mainly at the hanging wall of the fault and did not change significantly at the footwall (Aoyagi et al., 2021; Fukushima et al., 2013), consistent with the inference from the variations of ω . Therefore, we interpret the observed variations of width as the transient width adjustment to accelerated incision.

The width adjustment observed in this study differs from the adjustment observed in flume experiments by Baynes et al. (2022). While channel narrowing initiated downstream of the knickpoint in Iwaki, narrowing started upstream of the knickpoint (waterfall) in Baynes et al. (2022). They attributed the narrowing upstream of the knickpoint to the requirement of the channel to increase the bed shear stress in order to transport the material eroded from the knickpoint in addition to the sediment from upstream. In real landscapes, the rates of sediment supply might be increased around the knickpoint due to faster incision. However, the magnitude of the increased sediment supply around the knickpoint should be much less significant in real landscapes than in flume experiments due to the difference in upstream drainage area relative to the drainage area at the knickpoint.

Another difference in width adjustment between this study and previous studies (e.g., Baynes et al., 2022; Yanites, 2018) is that the evolution of channel width following the initial narrowing. In this study, channel width kept narrower after the passage of the knickpoints (Figures 4c and 4f). Baynes et al. (2022) reported that the

channel first narrowed and then became wider following the knickpoint passage. This shift from narrowing to widening corresponded with a transition from bed degradation to aggradation. Yanites (2018) modeled the evolution of channel slope and width following an increase in rock uplift rates based on the five erosion models that include and do not include the effects of sediment on erosion. The modeling results with sediment effects (the sediment cover detachment-limited model, tool- and exposure-limited saltation abrasion models) predicted initial channel narrowing followed by widening. However, the overall width changes (i.e., the sum of narrowing and widening) were negative in models of less pronounced sediment effects (the pure detachment limited model and sediment cover detachment limited model) among the five models. Based on the results of flume and numerical experiments (Baynes et al., 2022; Yanites, 2018; Yanites & Tucker, 2010), channel narrowing is more likely to occur under a detachment-limited condition and widening becomes more favorable as sediment supply increases relative to transport capacity. In Iwaki, although we do not have quantitative evidence of relative sediment supply, the presence of slope-break knickpoints and lack of strath and fill terraces in the basins where channel narrowing was observed suggest the streams were inclined to a detachment-limited condition and vertical erosion prevailed following knickpoint retreat. Therefore, the observation that overall changes in width were negative was reasonable. Yet, we cannot exclude the possibility that channel widening has occurred or will occur because the magnitude of widening after narrowing may be small (Yanites, 2018) and less than the measurement uncertainty. Therefore, constraints on relative sediment supply and more extensive width measurement are required for further understanding of the width evolution in response to accelerated incision.

We observed a relatively slow increase in hillslope angles following a more rapid and significant increase in hillslope angles at the initial stage of the adjustment (Figure 4). This gradual and relatively small increase in hillslope angles may be caused by channel widening (e.g., Baynes et al., 2022); however, channel widening was not observed in Iwaki. Instead, we argue that the gradual hillslope adjustment is related to the decay of rates of changes in hillslope angles. Following an increase in incision rates at hillslope toes, hillslope angles rapidly increase at the initial stage of the adjustment, and their rates of change gradually decrease (Roering et al., 2001). Also, when the initial hillslope angles are close to the threshold angle, the hillslope response occurs mainly at the upper part of the hillslope (Roering et al., 2007). In that case, the change in hillslope angles may not be evident in the variation of average hillslope angles along streams, which explains the lack of clear hillslope response in Basin 5 (Figure 4e) where the initial hillslope angle is large and the difference in the final and initial hillslope angles was minimum among the basins analyzed (Figure 5a).

Channel width adjustment can alter the length of adjacent hillslopes, causing changes in hillslope forms (e.g., Baynes et al., 2022). In Iwaki, hillslope angles are expected to decrease because the channel narrowing can increase the hillslope length, which was not observed downstream of the knickpoints (Figure 4). The apparent lack of the interaction of hillslope and channel width adjustments is probably because the magnitude of width adjustment was small (~5 m at most, Figure S5 in Supporting Information S1) relative to the hillslope length. We calculated the potential changes in hillslope angles caused by lateral channel adjustment using average hillslope length downstream of the knickpoint (Figures S13 and S14 in Supporting Information S1). Assuming that up to 5 m of width adjustment occurred symmetrically (i.e., same degree of width adjustment at the right and left banks), the changes in hillslope angles are less than 1° (Figure S14 in Supporting Information S1), within the natural variability in hillslope angles along the streams (Figure 4).

5.3. Implications for the Adjustment Timescale

Our approach using knickpoint travel times revealed the timescales of the evolution of channel width and hillslope angles following an increase in incision rates. The total adjustment times for width are on the order of $>10^5$ years, consistent with the results of numerical modeling (Yanites, 2018). Although the delay times for width and hillslope angles are similar in Basin 3, the adjustment timescale is probably longer for width than for hillslope angles (Figure 7). The hillslope adjustments consisted of an initial rapid adjustment followed by a more gradual and less significant adjustment. The initial rapid adjustment took <0.2 My in Basin 3 and <0.4 My in Basin 4 (Figure 7), consistent with the timescales predicted from soil transport models on hillslopes (Hurst et al., 2012; Roering et al., 2001). The full adjustment timescales of hillslope angles can be much longer than the timescale for the initial hillslope adjustment (Basin 6 in Figure 7). The difference in the timescales between the initial and full adjustment of hillslope angles is also shown by numerical models (Roering et al., 2001). Because the rate of change in hillslope angles decreases as the adjustment proceeds, the time required for hillslope angles to reach

the value at the final steady state is much longer than the time for hillslope angles to reach 90% of the final value (Roering et al., 2001). While the impacts of the hillslope-channel coupling on the hillslope angles were minimum in Iwaki, the changes in hillslope angles due to lateral channel adjustment cannot be ignored when the magnitude of width adjustment is large, which further prolongs the adjustment timescales of hillslope angles. These results indicate that the transient response takes place at different spatiotemporal scales for channel slope, channel width, and hillslope angle. Therefore, channel width and hillslope angles along a trunk and tributaries may continue to adjust even when the river lacks a prominent knickpoint. Since channel characteristics and hillslope morphology are the primary controls of river incision (e.g., Whipple & Tucker, 2002), correctly identifying the adjusted sections within a catchment is essential for assessing the transient response to an increase in incision rates.

6. Conclusions

We documented the variation of channel width and hillslope angles along the streams in response to an increase in incision rates. The transient width and hillslope response were diverse even under similar geologic and tectonic conditions, which partly result from local factors, such as sediment dynamics and human activities. Although we measured width and hillslope angles with a relatively high spatial density, more extensive measurements are required to discuss the evolution of width and hillslope angles against model predictions because the natural variability is large relative to the magnitude of width and hillslope adjustment. Also, we have estimated their adjustment times to accelerated incision using the knickpoint travel time. Our approach enabled us to estimate both delay and response times of channel width and hillslope angles, which are otherwise difficult to constrain in an actual landscape. Our results indicate that adjustment timescales for width are $>10^5$ years, which is not negligible compared to the adjustment time of channel slope. Hillslope adjustment may take a comparatively long time if the impact of width adjustment on hillslope angles is significant or we consider the gradual increase in hillslope angles at the latter stage of the adjustment. These results mean transient response of channel slope, width, and hillslope angles occur in different spatiotemporal scales, posing a challenge in discussing catchment-scale adjustment time. Lastly, it has to be noted that our estimates of knickpoint travel time do not explicitly consider important factors, such as the effects of sediment characteristics and temporal changes in precipitation. Because these factors may significantly alter estimates of adjustment time, inter-model comparisons or more sophisticated models of migrating knickpoints are necessary to understand the transient response of bedrock rivers.

Data Availability Statement

The data used in this study are available in Takahashi (2023) at PANGAEA via (doi: <https://doi.pangaea.de/10.1594/PANGAEA.961088>).

Acknowledgments

We thank Chia-Yu Chen (National Chung Cheng University) for helpful comments and A. Morikawa, K. Kitamura (Kyoto University), N. Miyauchi, and Y. Tsuchiya (The University of Tokyo) for their assistance during preparation of the ^{10}Be samples. This manuscript benefitted from thorough reviews and constructive comments by Alexander C. Whittaker, two anonymous reviewers, Associate Editor Adam M. Booth, and Editor Mikael Attal. This work was supported by the International Joint Graduate Program in Earth and Environmental Sciences, Tohoku University, and Earthquake Disaster Prevention for Urban Areas Lab in International Research Institute of Disaster Science, Tohoku University. N. Takahashi and R. Ohta thank the staff at Yunodake sanso in Iwaki for their generous support during our fieldwork. We obtained DEM data from the Geospatial Authority of Japan and NOAA (ETOPO1). Some color maps were obtained from Crameri (2018).

References

- Ahnert, F. (1970). Functional relationships between denudation, relief, and uplift in large mid-latitude drainage basins. *American Journal of Science*, 268(3), 243–263. <https://doi.org/10.2475/ajs.268.3.243>
- Allen, G. H., Barnes, J. B., Pavelsky, T. M., & Kirby, E. (2013). Lithologic and tectonic controls on bedrock channel form at the northwest Himalayan front. *Journal of Geophysical Research: Earth Surface*, 118(3), 1806–1825. <https://doi.org/10.1002/jgrf.20113>
- Amos, C. B., & Burbank, D. W. (2007). Channel width response to differential uplift. *Journal of Geophysical Research*, 112(F2), F02010. <https://doi.org/10.1029/2006JF000672>
- Aoyagi, Y., Kageshima, M., Onuma, T., Homma, S., & Mukoyama, S. (2021). Fault displacement of the 2011 Mw 6.6 Fukushima-ken Hamadori earthquake based on a 3D crustal deformation model constructed using differential InSAR–Lidar. *Bulletin of the Seismological Society of America*, 111(5), 2303–2316. <https://doi.org/10.1785/0120210035>
- Attal, M., Tucker, G. E., Whittaker, A. C., Cowie, P. A., & Roberts, G. P. (2008). Modelling fluvial incision and transient landscape evolution: Influence of dynamic Channel adjustment. *Journal of Geophysical Research*, 113(3), 1–16. <https://doi.org/10.1029/2007JF000893>
- Awata, Y. (1988). Shortening of the central inner arc of the northeast Japan and movement of the Pacific plate. *Chikyu Monthly*, 10(9), 586–591.
- Awata, Y., & Kakimi, T. (1985). Quaternary tectonics and damaging earthquakes in northeast Honshu, Japan. *Earthquake Prediction Research*, 3, 231–251.
- Baynes, E. R. C., Lague, D., Steer, P., & Davy, P. (2022). Dynamic bedrock channel width during knickpoint retreat enhances undercutting of coupled hillslopes. *Earth Surface Processes and Landforms*, 47(15), 3629–3640. <https://doi.org/10.1002/esp.5477>
- Bierman, P., & Steig, E. J. (1996). Estimating rates of denudation using cosmogenic isotope abundances in sediment. *Earth Surface Processes and Landforms*, 21(2), 125–139. [https://doi.org/10.1002/\(sici\)1096-9837\(199602\)21:2<125::aid-esp511>3.0.co;2-8](https://doi.org/10.1002/(sici)1096-9837(199602)21:2<125::aid-esp511>3.0.co;2-8)
- Braucher, R., Brown, E. T., Bourlès, D. L., & Colin, F. (2003). In situ produced ^{10}Be measurements at great depths: Implications for production rates by fast muons. *Earth and Planetary Science Letters*, 211(3–4), 251–258. [https://doi.org/10.1016/S0012-821X\(03\)00205-X](https://doi.org/10.1016/S0012-821X(03)00205-X)
- Brown, E. T., Bourlès, D. L., Colin, F., Raisbeck, G. M., Yiou, F., & Desgarceaux, S. (1995). Evidence for muon-induced production of ^{10}Be in near-surface rocks from the Congo. *Geophysical Research Letters*, 22(6), 703–706. <https://doi.org/10.1029/95GL00167>

- Brown, E. T., Stallard, R. F., Larsen, M. C., Raisbeck, G. M., & Yiou, F. (1995). Denudation rates determined from the accumulation of in situ-produced ^{10}Be in the luquillo experimental forest, Puerto Rico. *Earth and Planetary Science Letters*, 129(1–4), 193–202. [https://doi.org/10.1016/0012-821X\(94\)00249-X](https://doi.org/10.1016/0012-821X(94)00249-X)
- Chen, Y. W., Shyu, J. B. H., & Chang, C. P. (2015). Neotectonic characteristics along the eastern flank of the Central Range in the active Taiwan orogen inferred from fluvial channel morphology. *Tectonics*, 34(10), 2249–2270. <https://doi.org/10.1002/2014TC003795>
- Chmieleff, J., von Blanckenburg, F., Kossert, K., & Jakob, D. (2010). Determination of the ^{10}Be half-life by multicollector ICP-MS and liquid scintillation counting. *Nuclear Instruments and Methods in Physics Research Section B: Beam Interactions with Materials and Atoms*, 268(2), 192–199. <https://doi.org/10.1016/j.nimb.2009.09.012>
- Cramer, F. (2018). Scientific colour maps (Version 7.0.0). Zenodo. <https://doi.org/10.5281/ZENODO.1243862>
- Crosby, B. T., & Whipple, K. X. (2006). Knickpoint initiation and distribution within fluvial networks: 236 waterfalls in the Waipaoa river, north Island, New Zealand. *Geomorphology*, 82(1–2), 16–38. <https://doi.org/10.1016/j.geomorph.2005.08.023>
- Deal, E. (2021). *Downstream hydraulic geometry data compilation*. HydroShare. Retrieved from <http://www.hydroshare.org/resource/0629ffb81fdb40aa9e6be42cc11918ca>
- DiBiase, R. A., Heimsath, A. M., & Whipple, K. X. (2012). Hillslope response to tectonic forcing in threshold landscapes. *Earth Surface Processes and Landforms*, 37(8), 855–865. <https://doi.org/10.1002/esp.3205>
- DiBiase, R. A., Whipple, K. X., Lamb, M. P., & Heimsath, A. M. (2015). The role of waterfalls and knickzones in controlling the style and pace of landscape adjustment in the western San Gabriel Mountains, California. *Bulletin of the Geological Society of America*, 127(3–4), 539–559. <https://doi.org/10.1130/B31113.1>
- Doke, R., Tanikawa, S., Yasue, K., Nakayasu, A., Niizato, T., Umeda, K., & Tanaka, T. (2012). Spatial patterns of initiation ages of active faulting in the Japanese islands. *Active Fault Research*, 37, 1–15. https://doi.org/10.1146/afr.2012.37_1
- Ferguson, R. I., Sharma, B. P., Hardy, R. J., Hodge, R. A., & Warburton, J. (2017). Flow resistance and hydraulic geometry in contrasting reaches of a bedrock channel. *Water Resources Research*, 53(3), 2278–2293. <https://doi.org/10.1002/2016WR020233>
- Flint, J. J. (1974). Stream gradient as a function of order, magnitude, and discharge. *Water Resources Research*, 10(5), 969–973. <https://doi.org/10.1029/WR010i005p0969>
- Fukushima, Y., Takada, Y., & Hashimoto, M. (2013). Complex ruptures of the 11 April 2011 Mw 6.6 Iwaki earthquake triggered by the 11 March 2011 Mw 9.0 Tohoku earthquake, Japan. *Bulletin of the Seismological Society of America*, 103(2 B), 1572–1583. <https://doi.org/10.1785/0120120140>
- Gallen, S. F., & Wegmann, K. W. (2017). River profile response to normal fault growth and linkage: An example from the Hellenic forearc of south-central Crete, Greece. *Earth Surface Dynamics*, 5(1), 161–186. <https://doi.org/10.5194/esurf-5-161-2017>
- Gallen, S. F., Wegmann, K. W., Franke, K. L., Hughes, S., Lewis, R. Q., Lyons, N., et al. (2011). Hillslope response to knickpoint migration in the Southern Appalachians: Implications for the evolution of post-orogenic landscapes. *Earth Surface Processes and Landforms*, 36(9), 1254–1267. <https://doi.org/10.1002/esp.2150>
- Gelman, A., & Rubin, D. B. (1992). Inference from iterative simulation using multiple sequences. *Statistical Science*, 7(4), 457–472. <https://doi.org/10.1214/ss/1177011136>
- Geological Survey of Japan. (2020). *Seamless digital geological map of Japan*. Geological Survey of Japan. Retrieved from <https://gbank.gsj.jp/seamless/>
- Golly, A., Turowski, J. M., Badoux, A., & Hovius, N. (2017). Controls and feedbacks in the coupling of mountain channels and hillslopes. *Geology*, 45(4), 307–310. <https://doi.org/10.1130/G38831.1>
- Goren, L. (2016). A theoretical model for fluvial channel response time during time-dependent climatic and tectonic forcing and its inverse applications. *Geophysical Research Letters*, 43(20), 10753–10763. <https://doi.org/10.1002/2016GL070451>
- Goren, L., Willett, S. D., Herman, F., & Braun, J. (2014). Coupled numerical-analytical approach to landscape evolution modeling. *Earth Surface Processes and Landforms*, 39(4), 522–545. <https://doi.org/10.1002/esp.3514>
- Gosse, J. C., & Phillips, F. M. (2001). Terrestrial in situ cosmogenic nuclides: Theory and application. *Quaternary Science Reviews*, 20(14), 1475–1560. [https://doi.org/10.1016/S0277-3791\(00\)00171-2](https://doi.org/10.1016/S0277-3791(00)00171-2)
- Granger, D. E., Kirchner, J. W., & Finkel, R. (1996). Spatially averaged long-term erosion rates measured from in situ-produced cosmogenic nuclides in alluvial sediment. *The Journal of Geology*, 104(3), 249–257. <https://doi.org/10.1086/629823>
- Harel, M. A., Mudd, S. M., & Attal, M. (2016). Global analysis of the stream power law parameters based on worldwide ^{10}Be denudation rates. *Geomorphology*, 268, 184–196. <https://doi.org/10.1016/j.geomorph.2016.05.035>
- Hilley, G. E., Porder, S., Aron, F., Baden, C. W., Johnstone, S. A., Liu, F., et al. (2019). Earth's topographic relief potentially limited by an upper bound on channel steepness. *Nature Geoscience*, 12(10), 828–832. <https://doi.org/10.1038/s41561-019-0442-3>
- Hiroi, Y., Yokose, M., Oba, T., Kishi, S., Nohara, T., & Yao, A. (1987). Discovery of Jurassic radiolaria from acmite-rhodnite-bearing metachert of the Gosaisyo metamorphic rocks in the Abukuma terrane, northeastern Japan. *The Journal of the Geological Society of Japan*, 93(6), 445–448. <https://doi.org/10.5575/geosoc.93.445>
- Howard, A. D., & Kerby, G. (1983). Channel changes in badlands. *Geological Society of America Bulletin*, 94(6), 739–752. [https://doi.org/10.1130/0016-7606\(1983\)94<739:CCIB>2.0.CO;2](https://doi.org/10.1130/0016-7606(1983)94<739:CCIB>2.0.CO;2)
- Hurst, M. D., Grieve, S. W. D., Clubb, F. J., & Mudd, S. M. (2019). Detection of channel-hillslope coupling along a tectonic gradient. *Earth and Planetary Science Letters*, 522, 30–39. <https://doi.org/10.1016/j.epsl.2019.06.018>
- Hurst, M. D., Mudd, S. M., Walcott, R., Attal, M., & Yoo, K. (2012). Using hilltop curvature to derive the spatial distribution of erosion rates. *Journal of Geophysical Research*, 117(F2), F02017. <https://doi.org/10.1029/2011JF002057>
- Imanishi, K., Ando, R., & Kuwahara, Y. (2012). Unusual shallow normal-faulting earthquake sequence in compressional northeast Japan activated after the 2011 off the Pacific coast of Tohoku earthquake. *Geophysical Research Letters*, 39(9), L09306. <https://doi.org/10.1029/2012GL051491>
- Japan Meteorological Agency. (2021). Past meteorological data. Retrieved from <http://www.data.jma.go.jp/obd/stats/etrn/index.php>
- Kano, H., Kuroda, Y., Uruno, K., Nureki, T., Kanisawa, S., Maruyama, T., et al. (1973). *Geology of the Takanuki district (07-70, scale 1:50,000)*. Geological Survey of Japan.
- Kirby, E., & Whipple, K. X. (2012). Expression of active tectonics in erosional landscapes. *Journal of Structural Geology*, 44, 54–75. <https://doi.org/10.1016/j.jsg.2012.07.009>
- Kohl, C., & Nishiizumi, K. (1992). Chemical isolation of quartz for measurement of in-situ-produced cosmogenic nuclides. *Geochimica et Cosmochimica Acta*, 56(9), 3583–3587. [https://doi.org/10.1016/0016-7037\(92\)90401-4](https://doi.org/10.1016/0016-7037(92)90401-4)
- Korschinek, G., Bergmaier, A., Faestermann, T., Gerstmann, U. C., Knie, K., Rugel, G., et al. (2010). A new value for the half-life of ^{10}Be by heavy-ion elastic recoil detection and liquid scintillation counting. *Nuclear Instruments and Methods in Physics Research Section B: Beam Interactions with Materials and Atoms*, 268(2), 187–191. <https://doi.org/10.1016/j.nimb.2009.09.020>

- Kubo, K., & Yamamoto, T. (1990). Cretaceous intrusive rocks of the Haramachi district, eastern margin of the Abukuma Mountains. *The Journal of the Geological Society of Japan*, 96(9), 731–743. <https://doi.org/10.5575/geosoc.96.731>
- Kubo, K., Yanagisawa, Y., Yamamoto, T., Nakae, S., Takahashi, Y., Toshimitsu, S., et al. (2007). *Geological map of Japan, Shirakawa (NJ54-17-23, scale 1:200,000)*. Geological Survey of Japan.
- Lavé, J., & Avouac, J. P. (2001). Fluvial incision and tectonic uplift across the Himalayas of central Nepal. *Journal of Geophysical Research*, 106(B11), 26561–26591. <https://doi.org/10.1029/2001jb000359>
- Li, Y.-k. (2013). Determining topographic shielding from digital elevation models for cosmogenic nuclide analysis: A GIS approach and field validation. *Journal of Mountain Science*, 10(3), 355–362. <https://doi.org/10.1007/s11629-013-2564-1>
- Lindeløv, J. K. (2020). mcp: An R package for regression with multiple change points. *OSF Preprints*. <https://doi.org/10.31219/osf.io/fzqxv>
- Matsushi, Y., Matsuzaki, H., & Makino, H. (2014). Testing models of landform evolution by determining the denudation rates of mountains watersheds using terrestrial cosmogenic nuclides. *Transactions - Japanese Geomorphological Union*, 35(2), 165–185. <https://dl.ndl.go.jp/pid/10808840/1/1>
- Matsuzaki, H., Nakano, C., Tsuchiya, Y. S., Kato, K., Maejima, Y., Miyairi, Y., et al. (2007). Multi-nuclide AMS performances at MALT. *Nuclear Instruments and Methods in Physics Research Section B: Beam Interactions with Materials and Atoms*, 259(1), 36–40. <https://doi.org/10.1016/j.nimb.2007.01.145>
- Mitchell, N. A., & Yanites, B. J. (2019). Spatially variable increase in rock uplift in the northern U.S. Cordillera recorded in the distribution of river knickpoints and incision depths. *Journal of Geophysical Research: Earth Surface*, 124(5), 1238–1260. <https://doi.org/10.1029/2018JF004880>
- Mitsui, S. (1971). *Studies on the mechanism of deformation of sedimentary rocks in the Iwaki area of the Joban Coal-Field* (Vol. 42, pp. 199–272). The science reports of the Tohoku University. Second series, Geology. Retrieved from <http://hdl.handle.net/10097/28814>
- Miyashita, Y. (2018). Holocene paleoseismic history of the Yunodake fault ruptured by the 2011 Fukushima-ken Hamadori earthquake, Fukushima Prefecture, Japan. *Geomorphology*, 323, 70–79. <https://doi.org/10.1016/j.geomorph.2018.08.040>
- Montgomery, D. R., & Brandon, M. T. (2002). Topographic controls on erosion rates in tectonically active mountain ranges. *Earth and Planetary Science Letters*, 201(3–4), 481–489. [https://doi.org/10.1016/S0012-821X\(02\)00725-2](https://doi.org/10.1016/S0012-821X(02)00725-2)
- Montgomery, D. R., & Foufoula-Georgiou, E. (1993). Channel network source representation using digital elevation models. *Water Resources Research*, 29(12), 3925–3934. <https://doi.org/10.1029/93WR02463>
- Montgomery, D. R., & Gran, K. B. (2001). Downstream variations in the width of bedrock channels. *Water Resources Research*, 37(6), 1841–1846. <https://doi.org/10.1029/2000WR900393>
- Mudd, S. M., & Furbish, D. J. (2007). Responses of soil-mantled hillslopes to transient channel incision rates. *Journal of Geophysical Research*, 112(3), 1–12. <https://doi.org/10.1029/2006JF000516>
- Nakajima, T. (2013). Late Cenozoic tectonic events and intra-arc basin development in Northeast Japan. In Y. Itoh (Ed.), *Mechanism of sedimentary basin formation-multidisciplinary approach on active plate margins* (pp. 153–189). InTech. <https://doi.org/10.5772/56706>
- Nakajima, T. (2018). Tectonics of sedimentary basins in and around Japan since the opening of the Sea of Japan. *The Journal of the Geological Society of Japan*, 124(9), 693–722. <https://doi.org/10.5575/geosoc.2018.0049>
- Nakamura, A., Yokoyama, Y., Shiroya, K., Miyairi, Y., & Matsuzaki, H. (2014). Direct comparison of site-specific and basin-scale denudation rate estimation by in situ cosmogenic nuclides: An example from the Abukuma Mountains, Japan. *Progress in Earth and Planetary Science*, 1(1), 1–11. <https://doi.org/10.1186/2197-4284-1-9>
- Nakata, T. & Imaizumi, T. (Eds.) (2002). *Digital active fault map of Japan*. University of Tokyo press.
- Nishiizumi, K., Imamura, M., Caffee, M. W., Southon, J. R., Finkel, R. C., & McAninch, J. (2007). Absolute calibration of ^{10}Be AMS standards. *Nuclear Instruments and Methods in Physics Research Section B: Beam Interactions with Materials and Atoms*, 258(2), 403–413. <https://doi.org/10.1016/j.nimb.2007.01.297>
- Ouimet, W. B., Whipple, K. X., & Granger, D. E. (2009). Beyond threshold hillslopes: Channel adjustment to base-level fall in tectonically active mountain ranges. *Geology*, 37(7), 579–582. <https://doi.org/10.1130/G30013A.1>
- Perron, J. T., & Royden, L. (2013). An integral approach to bedrock river profile analysis. *Earth Surface Processes and Landforms*, 38(6), 570–576. <https://doi.org/10.1002/esp.3302>
- Petit, C., Goren, L., Rolland, Y., Bourlès, D., Braucher, R., Saillard, M., & Cassol, D. (2017). Recent, climate-driven river incision rate fluctuations in the Mercantour crystalline massif, southern French Alps. *Quaternary Science Reviews*, 165, 73–87. <https://doi.org/10.1016/j.quascirev.2017.04.015>
- R Core Team. (2022). *R: A language and environment for statistical computing*. R Foundation for Statistical Computing.
- Regalla, C., Kirby, E., Fisher, D., & Bierman, P. (2013). Active forearc shortening in Tohoku, Japan: Constraints on fault geometry from erosion rates and fluvial longitudinal profiles. *Geomorphology*, 195, 84–98. <https://doi.org/10.1016/j.geomorph.2013.04.029>
- Reinhardt, L. J., Bishop, P., Hoey, T. B., Dempster, T. J., & Sanderson, D. C. W. (2007). Quantification of the transient response to base-level fall in a small mountain catchment: Sierra Nevada, southern Spain. *Journal of Geophysical Research*, 112(F3), F03S05. <https://doi.org/10.1029/2006JF000524>
- Roering, J. J. (2008). How well can hillslope evolution models “explain” topography? Simulating soil transport and production with high-resolution topographic data. *Bulletin of the Geological Society of America*, 120(9–10), 1248–1262. <https://doi.org/10.1130/B26283.1>
- Roering, J. J., Kirchner, J. W., & Dietrich, W. E. (2001). Hillslope evolution by nonlinear, slope-dependent transport: Steady state morphology and equilibrium adjustment timescales. *Journal of Geophysical Research*, 106(B8), 16499–16513. <https://doi.org/10.1029/2001jb000323>
- Roering, J. J., Perron, J. T., & Kirchner, J. W. (2007). Functional relationships between denudation and hillslope form and relief. *Earth and Planetary Science Letters*, 264(1–2), 245–258. <https://doi.org/10.1016/j.epsl.2007.09.035>
- Royden, L., & Perron, J. T. (2013). Solutions of the stream power equation and application to the evolution of river longitudinal profiles. *Journal of Geophysical Research: Earth Surface*, 118(2), 497–518. <https://doi.org/10.1002/jgrf.20031>
- Rudge, J. F., Roberts, G. G., White, N. J., & Richardson, C. N. (2015). Uplift histories of Africa and Australia from linear inverse modeling of drainage inventories. *Journal of Geophysical Research: Earth Surface*, 120(5), 894–914. <https://doi.org/10.1002/2014JF003297>
- Schwanghart, W., & Scherler, D. (2014). Short communication: TopoToolbox 2—MATLAB-based software for topographic analysis and modeling in Earth surface sciences. *Earth Surface Dynamics*, 2(1), 1–7. <https://doi.org/10.5194/esurf-2-1-2014>
- Snyder, N. P., Whipple, K. X., Tucker, G. E., & Merritts, D. J. (2000). Landscape response to tectonic forcing: Digital elevation model analysis of stream profiles in the Mendocino triple junction region, Northern California. *Bulletin of the Geological Society of America*, 112(8), 1250–1263. [https://doi.org/10.1130/0016-7606\(2000\)112<1250:LRTTFD>2.0.CO;2](https://doi.org/10.1130/0016-7606(2000)112<1250:LRTTFD>2.0.CO;2)
- Snyder, N. P., Whipple, K. X., Tucker, G. E., & Merritts, D. J. (2003). Channel response to tectonic forcing: Field analysis of stream morphology and hydrology in the Mendocino triple junction region, northern California. *Geomorphology*, 53(1–2), 97–127. [https://doi.org/10.1016/S0169-555X\(02\)00349-5](https://doi.org/10.1016/S0169-555X(02)00349-5)

- Stock, J., & Dietrich, W. E. (2003). Valley incision by debris flows: Evidence of a topographic signature. *Water Resources Research*, 39(4), 1089. <https://doi.org/10.1029/2001WR001057>
- Stone, J. O. (2000). Air pressure and cosmogenic isotope production. *Journal of Geophysical Research*, 105(B10), 23753–23759. <https://doi.org/10.1029/2000jb900181>
- Takahashi, N. (2023). *Channel slope, flow width, flow depth, hillslope angle, unit stream power for the trunk streams in Iwaki*. PANGAEA. Retrieved from <https://doi.pangaea.de/10.1594/PANGAEA.961088>
- Toda, S., & Tsutsumi, H. (2013). Simultaneous reactivation of two, subparallel, inland normal faults during the Mw 6.6 11 April 2011 Iwaki earthquake triggered by the Mw 9.0 Tohoku-Oki, Japan, Earthquake. *Bulletin of the Seismological Society of America*, 103(2 B), 1584–1602. <https://doi.org/10.1785/0120120281>
- Turowski, J. M. (2020). Mass balance, grade, and adjustment timescales in bedrock channels. *Earth Surface Dynamics*, 8(1), 103–122. <https://doi.org/10.5194/esurf-8-103-2020>
- Wang, Y., Goren, L., Zheng, D., & Zhang, H. (2022). Short communication: Forward and inverse analytic models relating river long profile to tectonic uplift history, assuming a nonlinear slope-erosion dependency. *Earth Surface Dynamics*, 10(4), 833–849. <https://doi.org/10.5194/esurf-10-833-2022>
- Whipple, K. X. (2004). Bedrock Rivers and the geomorphology of active orogens. *Annual Review of Earth and Planetary Sciences*, 32(1), 151–185. <https://doi.org/10.1146/annurev.earth.32.101802.120356>
- Whipple, K. X., DiBiase, R. A., & Crosby, B. T. (2013). Bedrock rivers. In J. Shroder & E. Wohl (Eds.), *Treatise on geomorphology* (Vol. 9, pp. 550–573). Academic Press. <https://doi.org/10.1016/B978-0-12-374739-6.00254-2>
- Whipple, K. X., Hancock, G. S., & Anderson, R. S. (2000). River incision into bedrock: Mechanics and relative efficacy of plucking, abrasion, and cavitation. *Bulletin of the Geological Society of America*, 112(3), 490–503. [https://doi.org/10.1130/0016-7606\(2000\)112<490:RIIBMA>2.0.CO;2](https://doi.org/10.1130/0016-7606(2000)112<490:RIIBMA>2.0.CO;2)
- Whipple, K. X., & Tucker, G. E. (1999). Dynamics of the stream-power river incision model: Implications for height limits of mountain ranges, landscape response timescales, and research needs. *Journal of Geophysical Research*, 104(B8), 17661–17674. <https://doi.org/10.1029/1999jb900120>
- Whipple, K. X., & Tucker, G. E. (2002). Implications of sediment-flux-dependent river incision models for landscape evolution. *Journal of Geophysical Research*, 107(B2), 2039. <https://doi.org/10.1029/2000jb000044>
- Whittaker, A. C., & Boulton, S. J. (2012). Tectonic and climatic controls on knickpoint retreat rates and landscape response times. *Journal of Geophysical Research*, 117(F2), F02024. <https://doi.org/10.1029/2011JF002157>
- Whittaker, A. C., Cowie, P. A., Attal, M., Tucker, G. E., & Roberts, G. P. (2007). Contrasting transient and steady-state rivers crossing active normal faults: New field observations from the Central Apennines, Italy. *Basin Research*, 19(4), 529–556. <https://doi.org/10.1111/j.1365-2117.2007.00337.x>
- Wobus, C. W., Whipple, K. X., Kirby, E., Snyder, N., Johnson, J., Spyropolou, K., et al. (2006). Tectonics from topography: Procedures, promise, and pitfalls. *Special Paper 398: Tectonics, Climate, and Landscape Evolution*, 398, 55–74. [https://doi.org/10.1130/2006.2398\(04\)](https://doi.org/10.1130/2006.2398(04))
- Yanites, B. J. (2018). The dynamics of channel slope, width, and sediment in actively eroding bedrock river systems. *Journal of Geophysical Research: Earth Surface*, 123(7), 1504–1527. <https://doi.org/10.1029/2017JF004405>
- Yanites, B. J., & Tucker, G. E. (2010). Controls and limits on bedrock channel geometry. *Journal of Geophysical Research*, 115(F4), F04019. <https://doi.org/10.1029/2009JF001601>
- Yochum, S. E., Bledsoe, B. P., David, G. C. L., & Wohl, E. (2012). Velocity prediction in high-gradient channels. *Journal of Hydrology*, 424(425), 84–98. <https://doi.org/10.1016/j.jhydrol.2011.12.031>
- Yochum, S. E., Comiti, F., Wohl, E., David, G. C. L., & Mao, L. (2014). *Photographic guidance for selecting flow resistance coefficients in high-gradient channels*. USDA Forest Service—General Technical Report RMRS-GTR. <https://doi.org/10.2737/RMRS-GTR-323>
- Zhang, H., Kirby, E., Pitlick, J., Anderson, R. S., & Zhang, P. (2017). Characterizing the transient geomorphic response to base-level fall in the northeastern Tibetan Plateau. *Journal of Geophysical Research: Earth Surface*, 122(2), 546–572. <https://doi.org/10.1002/2015JF003715>